

Dark Energy and Neutrino Masses from Future Measurements of the Expansion History and Growth of Structure

Shahab Joudaki, Manoj Kaplinghat

Center for Cosmology, Dept. of Physics & Astronomy, University of California, Irvine, CA 92697

(Dated: June 8, 2018)

We forecast the expected cosmological constraints from a combination of probes of both the universal expansion rate and matter perturbation growth, in the form of weak lensing tomography, galaxy tomography, supernovae, and the cosmic microwave background incorporating all cross-correlations between the observables for an extensive cosmological parameter set. We allow for non-zero curvature and parameterize our ignorance of the early universe by allowing for a non-negligible fraction of dark energy (DE) at high redshifts. We find that early DE density can be constrained to 0.2% of the critical density of the universe with Planck combined with a ground-based LSST-like survey, while curvature can be constrained to 0.06%. However, these additional degrees of freedom degrade our ability to measure late-time dark energy and the sum of neutrino masses. We find that the combination of cosmological probes can break degeneracies and constrain the sum of neutrino masses to 0.04 eV, present DE density also to 0.2% of the critical density, and the equation of state to 0.01 – roughly a factor of two degradation in the constraints overall compared to the case without allowing for early DE. The constraints for a space-based mission are similar. Even a modest 1% dark energy fraction of the critical density at high redshift, if not accounted for in future analyses, biases the cosmological parameters by up to 2σ . Our analysis suggests that throwing out nonlinear scales (multipoles > 1000) may not result in significant degradation in future parameter measurements when multiple cosmological probes are combined. We find that including cross-correlations between the different probes can result in improved constraints by up to a factor of 2 for the sum of neutrino masses and early dark energy density.

I. INTRODUCTION

The measurement of the low-redshift expansion history through observations of SNIa [1, 2], combined with cosmic microwave background (CMB) observations of flatness [3, 4] and large-scale structure (LSS) measurements of a sub-critical matter density [5–7] provide strong arguments for a currently accelerating phase in the expansion of the universe. The simplest solution to these observations is provided by a cosmological constant, or a uniformly smooth vacuum energy, with a pressure that is the negative of the energy density.

Among alternatives to the cosmological constant, the most popular are scalar field models with potentials tailored to give rise to late-time acceleration and current equation of state for the dark energy, w , close to -1 [8–15]. These models are fine-tuned to have dark energy dominate today, just like the cosmological constant. However, the requirement $w \gtrsim -1$ currently, does not imply that dark energy was sub-dominant at earlier times, specifically redshift $z \gtrsim 2$, where we have no direct constraints. Even in single scalar field models, one could have a wide range of behavior for $w(z)$, or equivalently the evolution of the dark energy density with redshift. For example, oscillating $w(z)$ models provide an example where the dark energy density is not negligible in the past, while at the same time the fine-tuning of the potential is benign as compared to anthropic considerations [16].

Observationally, we have no direct constraints on the expansion rate of the universe at $z \gtrsim 2$. One way to parameterize our ignorance is to allow for early

dark energy. Such a parameterization also allows us to estimate the changes in the growth of structure compared to a Λ CDM model.

Our aim in this paper is three-fold.

1. We explore how well the present dark energy density and its equation of state may be constrained using multiple probes that are sensitive to the growth of structure and expansion history. *We include cross-correlations between these different probes and isolate their effect on parameter constraints and degeneracies.*
2. We include non-negligible dark energy density at early times ($z \gtrsim 2$), ask how well this contribution can be measured, and how it affects the inferred values for the present dark energy equation of state w and density Ω_{d0} .
3. We discuss how the inclusion of early dark energy affects the determination of the sum of the neutrino masses in spatially flat and non-flat cosmological models, along with the expected degradation from unknown reionization history.

With respect to the second point above, we note that a study of expected constraints from baryon acoustic oscillation (BAO) observations has shown that the presence of early dark energy can significantly bias the inferred values of late-time dark energy parameters [17]. We may attempt to resolve this bias by using a calibration parameter, similar to that for SNe observations. However, this would lead to more than a factor of two larger degradation in BAO dark energy

constraints [17], which stresses the importance of including this uncertainty in parameter constraints and on measuring dark energy contribution to the expansion rate at $z \gtrsim 2$.

At low redshift, the expansion rate in a model with EDE is designed to masquerade that of models with late-time ($z \lesssim 1$) dark energy [18], thereby severely limiting the constraining ability of probes exclusively sensitive to the universal expansion, such as SN measurements. The handle on early dark energy must therefore come from a combination of expansion rate and matter power spectrum measurements.

For a universe with dark energy to produce the matter perturbations seen in the present universe, more structure needed to have formed at earlier times than for a universe without dark energy. Similarly, a universe with a non-vanishing amount of dark energy at early times requires more structure to have formed at earlier times than a universe with only late-time dark energy. With a fixed large-scale normalization of the power spectrum, this implies a suppression of the matter power spectrum on small scales.

Another effect on small scales is due to massive neutrinos. These relativistic massive neutrinos can stream out of high-density regions on scales below the free-streaming length scale, and therefore suppress the perturbations in the small-scale matter spectrum. Both the free-streaming of neutrinos and the suppression of small-scale power due to dark energy are late-time effects. However, their effects may be disentangled in either the CMB lensing power spectrum [19, 20], shear power spectrum [21–23], or galaxy power spectrum [24–27] (moreover see Ref. [28] for a combined lensing analysis). We revisit this issue including the presence of early dark energy because we expect significant degeneracy between the effects of massive neutrinos and early dark energy [29].

Previous efforts to constrain models of early dark energy have focused on measurements of the CMB temperature and polarization fields, large and small scale structure formation, Lyman- α forest, Gamma-Ray Bursts, and SNe [30–35]. In recent work, the influence of weak gravitational lensing observations of galactic sources at low redshifts and the CMB as a large redshift source has also been investigated [29, 36]. In this work, we explore how well a generic model for dark energy that does not vanish at early times can be constrained in conjunction with massive neutrinos from a comprehensive array of next-generation weak lensing, galaxy, CMB (including lensing), and SN observations, including all cross-correlations between the non-SN probes. We include SNe to help break the degeneracies with the late-time dark energy parameters. It is worth noting that the comprehensive inclusion of cross-correlations is new even for the case with just late-time dark energy.

We take our fiducial cosmological model to be flat with a nonzero fraction of dark energy at high redshift, $\Omega_e = 0.01$, as discussed in the next section. We

assume that the dynamics is described by a canonical scalar field. In agreement with WMAP data [3, 4], we set $\Omega_{d0} = 0.742$, $w_0 = -1.0$, (present dark energy density and equation of state), $\Omega_c h^2 = 0.11$ (density of cold dark matter), $\Omega_b h^2 = 0.0227$ (density of baryons), $\Omega_\nu h^2 = 1.81 \times 10^{-3}$ (density of neutrino), $\Omega_k = 0$ (flatness), $n_s = 0.963$ (tilt of power spectrum), $dn_s/d \ln k = 0$ (running of tilt), $\Delta_R^2 = 2.21 \times 10^{-9}$ (normalization of power spectrum), $\tau = 0.087$ (optical depth to Thomson scattering), $N_{\text{eff}} = 3.04$ (effective number of neutrinos).

The fiducial value of $\Omega_\nu h^2$ corresponds to $\sum m_\nu = 94 \Omega_\nu h^2 \text{eV} = 0.17 \text{eV}$. For the inverted hierarchy, this value for the sum of neutrino masses actually implies 2 mass eigenstates with masses about 0.065 eV each and a lighter eigenstate. We have approximated this as 2 massive neutrino eigenstates (with masses 0.085 eV each) and one massless neutrino eigenstate. We included the fraction of $\sum m_\nu$ in one of the two massive eigenstates as a parameter $f_{\nu 1}$ but found that the Fisher matrix constraint on that fraction to be $\sim 1/2$ with all the cosmological probes and parameters included. Therefore, our results are not expected to change if, for example, we split $\sum m_\nu$ among 3 mass eigenstates. For brevity, we do not show this fraction parameter in the tables and figures. Even though cosmology is primarily sensitive to the sum of neutrino mass eigenstates, it can probe the neutrino mass hierarchy in the sense that if the sum of the neutrino mass is below 0.095 eV (see Fig. 11), then the normal hierarchy is the only solution [37].

It is important to note that our cosmological model above includes information about reionization only through the optical depth. This is sufficient if reionization happens rapidly enough compared to the age of the universe during reionization. However, the reionization process could be more gradual or more complicated (for example, occur in two stages) and this would manifest itself in a range of effects on the large-angle CMB polarization even when the optical depth is fixed [38]. As a result, the estimate of how well τ can be measured is dependent on the features of global reionization [38–40].

The constraint on τ determines how well the amplitude of the primordial power spectrum is measured such that $\sigma(\Delta_R^2)/\Delta_R^2 = 2\sigma(\tau)$, where $\sigma(X)$ denotes the uncertainty in parameter X . For constraints on parameters such as neutrino mass, the knowledge of the overall power spectrum normalization is important [19]. Here, we test the effect that including a detailed reionization model would have by imposing a floor on τ as advocated in Refs. [19, 39, 40]. The main results we quote in this paper, however, assume a sharp reionization scenario because our main aim is to see how adding different probes helps break degeneracies in the presence of an unknown dark energy component at high redshift.

We describe our method to include early dark energy in Section 2, reviewing the nonlinear matter

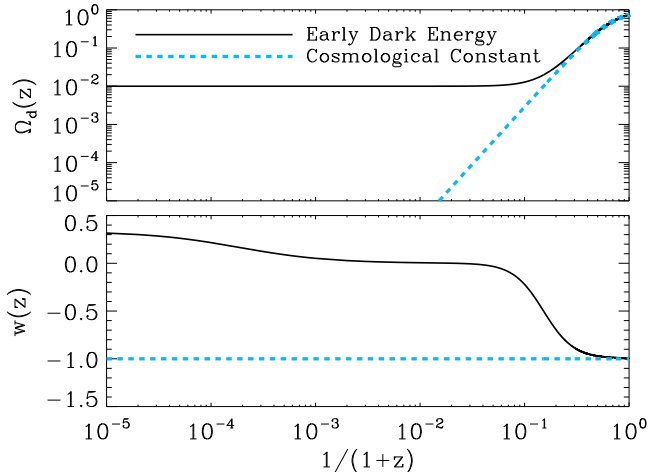


FIG. 1. Energy density (top) and equation of state (bottom) of early dark energy and a cosmological constant. At low redshifts the EDE mimics a dark energy component with the same density and EOS at present, and decouples after redshifts of a few, the exact redshift depending on the size of the EDE fraction Ω_e .

power spectrum, weak lensing power spectrum, galaxy power spectrum, SN distances, and the CMB. In Section 3, we provide prospective early dark energy and sum of neutrino mass constraints (and potential biases) obtained from a joint analysis of these probes, based on a Fisher matrix prescription. Section 4 concludes with a discussion of our findings.

II. METHODOLOGY

We begin with an overview of our calculation. We briefly describe the EDE cosmological model, and then discuss the relevant observational variables.

A. Early Dark Energy

Early dark energy changes the expansion rate and hence cosmological distances. It also changes the growth of density fluctuations in the universe and hence the matter power spectrum [16].

We begin by expressing the expansion rate of the universe in terms of the dark energy density $\Omega_d(z)$ (in units of the critical density) as

$$H(z) = H_0 \sqrt{\frac{\Omega_r(1+z)^4 + \Omega_m(1+z)^3 + \Omega_k(1+z)^2}{1 - \Omega_d(z)}}, \quad (1)$$

where $H_0 = 100 h \text{ km s}^{-1} \text{ Mpc}^{-1}$ is the Hubble constant, and $\{\Omega_r, \Omega_m, \Omega_k\}$ are the present radiation, matter, and curvature densities in units of the critical density. The present matter density is further composed of the densities of the cold dark matter, baryons,

and massive neutrinos ($\Omega_m = \Omega_c + \Omega_b + \Omega_\nu$). The evolution of dark energy is conventionally expressed as a function of its equation of state (EOS), $w(z)$,

$$\Omega_d(z) = \frac{\Omega_{d0} H_0^2}{H^2(z)} \exp\left(3 \int_0^z dz \frac{1+w(z)}{1+z}\right), \quad (2)$$

where $\Omega_{d0} = \Omega_d(0)$ is the present density of the dark energy.

A uniform and constant vacuum density ($w = -1$) is simple but suffers from the well-known coincidence problem. The value of the dark energy density has to be fine-tuned so that it only affects the dynamics of the universe at present. This coincidence problem motivates the exploration of solutions other than Λ CDM (e.g. [10, 41]). Among the possibilities that allow for $w > -1$ are models in which the evolution of the dark energy density is such that it is large enough to affect the universal dynamics even at $z > 2$. They may even alleviate the coincidence problem [16, 42].

A realization of early dark energy is given by the "tracker" parameterization of Doran & Robbers (2006) [18], where the dark energy tracks the dominant component in the universe. For this case, it is simpler to parameterize the dark energy density evolution directly, rather than express it in terms of an evolving equation of state. We use a modified form of the Doran and Robbers (2006) [18] parameterization that tracks the equation of state of the dominant energy, as shown in Fig. 1,

$$\begin{aligned} \Omega_d(z) &= \Omega_{d0} \frac{(1+z)^{3+3w_0}}{h_w^2(z)} \\ &+ \Omega_e v(z) \left(1 - \frac{(1+z)^{3+3w_0}}{h_w^2(z)}\right), \quad (3) \\ h_w^2(z) &= \Omega_{d0}(1+z)^{3+3w_0} + \Omega_m(1+z)^3 \\ &+ \Omega_r(1+z)^4 + \Omega_k(1+z)^2, \end{aligned}$$

where $w_0 = w(0)$. The function $v(z)$ should have the properties that it asymptotes to unity at large redshift and $v(0) = 0$, thus ensuring that $\Omega_d(z)$ asymptotes to Ω_e at large redshift and $\Omega_d(0) = \Omega_{d0}$. We use $v(z) = 1 - (1+z)^{3w_0}$ [18], but any other parameterization such that $d \ln(v)/d \ln(z) = \mathcal{O}(1)$ will give similar results. Note that the first term proportional to Ω_{d0} is dark energy density as a function of redshift for a model with present density of dark energy Ω_{d0} and constant EOS w_0 . Thus, in this parameterization with early dark energy, the effect at low redshift is the same as a model with constant EOS model w_0 and density Ω_{d0} . Quantitatively, the Ω_e term ("early dark energy") in Eqn. 3 constitutes [0, 2.1, 8.0, 17.7]% at redshifts $z = [0, 1, 2, 3]$ respectively of the overall amount of dark energy $\Omega_d(z)$ for $w = -1$ and $\Omega_e = 0.01$.

We may compute the EOS using the expression $w(z) = -1 + \frac{(1+z)}{z} \frac{d \ln[\Omega_d(z) H^2(z)]}{3 d \ln z}$. At $z=0$, $w(z) = w_0$ and increases with z , tending to 0 if the dominant component of energy density is due to pressureless matter and an example of this behavior is shown in Fig. 1.

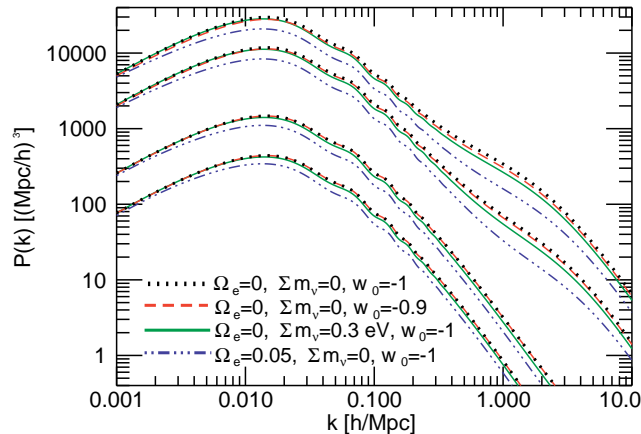


FIG. 2. Matter power spectrum $P(k)$ ($(\text{Mpc}/h)^3$) against wavenumber k (h/Mpc) at $z = [0, 1, 5, 10]$ (high to low) in four distinct cosmologies: ΛCDM (dotted black), $w\text{CDM}$ (dashed red, $w_0 = -0.9$ and $\Omega_e = 0$), ΛCDM with massive neutrinos (solid green, $\sum m_\nu = 0.3$ eV, $w_0 = -1$), and a CDM universe with EDE (dot-dashed blue, $\Omega_e = 0.05$, $w_0 = -1$).

B. Matter Power Spectrum

Given a particular parameterization of the EOS, the growth history depends on the underlying microphysical model for dark energy. In this paper, we will assume that the underlying model is a single scalar field. Then each $\Omega_d(z)$ or equivalently $w(z)$ can be connected to an underlying scalar field potential and equations for perturbations in matter, radiation and dark energy may be written down (e.g. [8, 43, 44].) This allows the calculation of the growth of matter perturbations. In order to correctly calculate the linear matter power spectrum, we numerically solve the Boltzmann equations with a modified version of CAMB [79]. We approximate the effect of an EDE component on the linear matter power spectrum by use of the PPF module by W. Fang [45, 46].

We extend this power spectrum to nonlinear scales by calculating the appropriate effective spectral index, effective spectral curvature, and nonlinear scale, and employing the fitting functions provided in Smith et al. (2001) [47]. The underlying cosmology in the Smith et al. fitting function manifests itself in two distinct ways. First, cosmology impacts the evolution of the matter density, $\Omega_m(z)$, and the evolution of the growth of matter perturbations, $D(z)$. The cosmology then fixes the functional form and coefficients associated with the fitting functions, which are fine-tuned to a suite of ΛCDM N-body simulations.

Thus, whereas an arbitrary dark energy EOS could leave its imprint on the nonlinear matter power spectrum via its influence on $\Omega_m(z)$ and $D(z)$, the cosmological dependence of the N-body fitting functions remain fine-tuned to a $w \equiv -1$ dark energy EOS. For this reason, the nonlinear solution for a non- ΛCDM cosmology is only approximate, and studies

have shown that it could lead to an underestimation of dark energy constraints: for example, in prospective weak lensing measurements by factor of two [48, 49]. Our use of this nonlinear extension could also underestimate the suppression of the matter power spectrum on small scales due to massive neutrinos (e.g. Ref [50]). Our constraints on neutrino mass, in particular from weak lensing, may therefore be conservative. Further work is needed to quantify this effect to the level of precision required for the next-generation telescopes considered in this paper (however, also see Refs. [51–53]).

Fig. 2 illustrates the matter power spectrum in four distinct cosmologies: ΛCDM , $w\text{CDM}$, ΛCDM with massive neutrinos, and a CDM universe with EDE. The inclusion of massive neutrinos induces a suppression of the matter power spectrum on scales below the free streaming length and this is, to an extent, degenerate with the suppression introduced by early dark energy. The suppression due to the presence of early dark energy is evident in Fig. 2 and is a result of the fact that the universe is expanding faster compared to a model with no early dark energy. The present (Ω_{d0}) and early ($\Omega_e \neq 0$) dark energy densities are further degenerate with the present DE equation of state w_0 . A combination of large and small scale probes are therefore needed to break the degeneracy between these cosmological parameters ($m_\nu, \Omega_{d0}, w_0, \Omega_e$) [23, 31, 36, 54].

C. Weak Lensing Tomography

The images of distant galaxies are gravitationally lensed by matter inhomogeneities along the line-of-sight. In the weak lensing regime these percent-level magnifications and shape distortions of galaxies need to be analyzed statistically (see [55, 56] for a review). By extracting the shear power spectrum of weakly lensed sources [57–65], the nature of the dark energy has been constrained with lensing surveys [58, 59]. An important aspect is that the lensing power spectrum depends on both the lensing kernel and the growth of perturbations, making lensing the most powerful probe of the underlying cosmology [66].

We employ weak lensing tomography, as this provides information about the redshift distribution of the intervening lenses, and thereby allows for more stringent constraints on cosmological parameters [67, 68]. We work within the Born approximation [69–71] to compute the lensing potential (weighted projection of the three-dimensional gravitational potential [72, 73]):

$$\phi_i(\hat{\mathbf{n}}) = \int_0^{z_{\text{max}}} dz K(z) \zeta_i^{\kappa}(z) \Phi(\hat{\mathbf{n}}, z), \quad (4)$$

where $K(z) \equiv H(z) d\chi/dz = 1$ in a flat universe. The lensing weight function (see Fig. 3) of the i^{th} tomo-

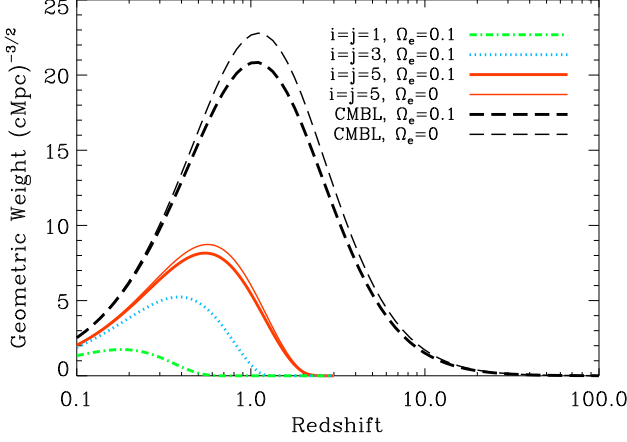


FIG. 3. Redshift dependent geometric weight $W_{ij}(z) = \frac{9}{16}(\Omega_m H_0^2)^2 H(z) \chi^{7/2}(z) \zeta_i^\kappa(z) \zeta_j^\kappa(z)$ (see text following Eqn. 13) of CMB weak lensing (CMBL) and tomographic low redshift weak lensing bins for a flat CDM model with $\Omega_e = 0.1$ and $w_0 = -1.0$. For CMB lensing and the fifth tomographic bin we also plot the kernel for $\Omega_e = 0$. The lensing kernel captures approximately the redshift dependence of the integrand for the lensing power spectrum (including that from the matter power spectrum). The diminishment of the kernels for $\Omega_e > 0$ stems from the increase of $H(z)$ with increasing Ω_e .

graphic bin is given by

$$\zeta_i^\kappa(z) = \frac{-2H^{-1}(z)}{\bar{n}_i \chi(z)} \int_{\max(z, z_i)}^{z_{i+1}} dz_s \frac{X(z, z_s) \rho(z_s)}{\chi(z_s)}, \quad (5)$$

$$X(z_o, z_s) = \frac{H_0^{-1}}{\sqrt{|\Omega_k|}} S_k \left(\sqrt{|\Omega_k|} \int_{z_o}^{z_s} dz' \frac{H_0}{H(z')} \right), \quad (6)$$

where $X(z_o, z_s)$ is the comoving distance to object at redshift z_s measured by observer at redshift z_o , such that $\chi(z) \equiv X(0, z)$, and $S_k(x) = [\sin(x), \sinh(x), x]$ for a [closed, open, flat] universe, respectively. We set $\zeta_i^\kappa(z) = 0$ explicitly if $z > z_{i+1}$. The quantity $\rho(z_s)$ contains the source galaxy distribution, the integral over which is \bar{n}_i (see Sec. III A). For the lensing of the CMB photons, we replace the galaxy source distribution with a δ -function at the last scattering surface.

The cross correlation of the respective Fourier coefficients at angular multipoles \mathbf{l} and \mathbf{l}' is given by

$$\langle \phi_i^*(\mathbf{l}) \phi_j(\mathbf{l}') \rangle = (2\pi)^2 \delta_{\mathbf{D}}(\mathbf{l} - \mathbf{l}') C_{ij}^{\phi\phi}(\ell) \quad (7)$$

in the flat sky limit, which through the Limber approximation reduces to [73–75]:

$$C_{ij}^{\phi\phi}(\ell) = \int_0^{z_{\max}} dz K(z) \zeta_i^\kappa(z) \zeta_j^\kappa(z) \frac{H(z)}{\chi^2(z)} P_{\Phi\Phi}(k, z). \quad (8)$$

This projected spectrum remains the same in the all sky formulation [72].

To find the relation between the power spectrum of the potential ($P_{\Phi\Phi}(\mathbf{k}, z)$) and matter perturbations ($P_{\delta\delta}(\mathbf{k}, z)$) on sub-horizon scales, we use the Poisson

equation in Fourier space,

$$\Phi(\mathbf{k}, z) = -\frac{3}{2} \Omega_m \left(\frac{H_0}{k} \right)^2 \delta(\mathbf{k}, z) (1+z). \quad (9)$$

Accounting for the definition of two-point correlations of the potential and density fields:

$$\begin{aligned} \langle \Phi^*(\mathbf{k}, z) \Phi(\mathbf{k}', z) \rangle &= (2\pi)^3 \delta_{\mathbf{D}}(\mathbf{k} - \mathbf{k}') P_{\Phi\Phi}(k, z), \\ \langle \delta^*(\mathbf{k}, z) \delta(\mathbf{k}', z) \rangle &= (2\pi)^3 \delta_{\mathbf{D}}(\mathbf{k} - \mathbf{k}') P_{\delta\delta}(k, z), \end{aligned} \quad (10)$$

we obtain the power spectrum of the potential in terms of the power spectrum of density fluctuations as

$$P_{\Phi\Phi}(k, z) = \frac{9}{4} \Omega_m^2 (1+z)^2 \left(\frac{H_0}{k} \right)^4 P_{\delta\delta}(k, z). \quad (11)$$

Reexpressing the power spectrum of the matter as a dimensionless quantity,

$$\Delta_{\delta\delta}^2(k, z) = k^3 P_{\delta\delta}(k, z) / (2\pi^2), \quad (12)$$

the spectrum of the convergence field, $C_\ell^{\kappa\kappa} = (1/4) \ell^2 (\ell+1)^2 C_\ell^{\phi\phi}$, is given by:

$$\begin{aligned} C_{ij}^{\kappa\kappa}(\ell) &= A_\ell^{\kappa\kappa} \int_0^{z_{\max}} dz K(z) \zeta_i^\kappa(z) \zeta_j^\kappa(z) \times \\ &(1+z)^2 H(z) \chi^5(z) \Delta_{\delta\delta}^2 \left(\frac{\ell+1/2}{\chi(z)}, z \right), \end{aligned} \quad (13)$$

where the density and scale dependent amplitude $A_\ell^{\kappa\kappa} = (9\pi^2/8) (\Omega_m H_0^2)^2 \ell^2 (\ell+1)^2 (\ell+1/2)^{-7}$, and $\Delta_{\delta\delta}^2(\ell/\chi(z), z)$ encapsulates the full nonlinear dark matter power spectrum. We construct a geometric weight $W_{ij}(z)$ that approximately captures the contribution to the convergence power spectrum from different redshifts for a broad range of multipoles by removing a factor of $(1+z)^2 \chi^{3/2}(z)$ from the integrand in Eqn 13. This results in $W_{ij}(z) = \frac{9}{16} (\Omega_m H_0^2)^2 H(z) \chi^{7/2}(z) \zeta_i^\kappa(z) \zeta_j^\kappa(z)$. The reason this approximation takes into account the redshift contribution to the convergence power spectrum is that the matter power spectrum $\Delta_{\delta\delta}^2(k, z)$ scales roughly like $k^{3/2}$ for scales $\mathcal{O}(0.1/\text{Mpc})$. We plot this geometric weight $W_{ij}(z)$ in Fig. 3, and this shows that most of the contribution to low redshift weak lensing comes from $z \approx 0.5$, and in the case of CMB weak lensing $z \approx 1$.

Fig. 4 further illustrates the effect of varying the dark energy and other parameters on the correlation function in the third tomographic bin. The shapes are roughly the same across the other bins. The similarity in the shapes of the variation due to early dark energy and sum of neutrino masses implies that there will be a degradation in the constraints on the sum of neutrino masses due to the addition of early dark energy.

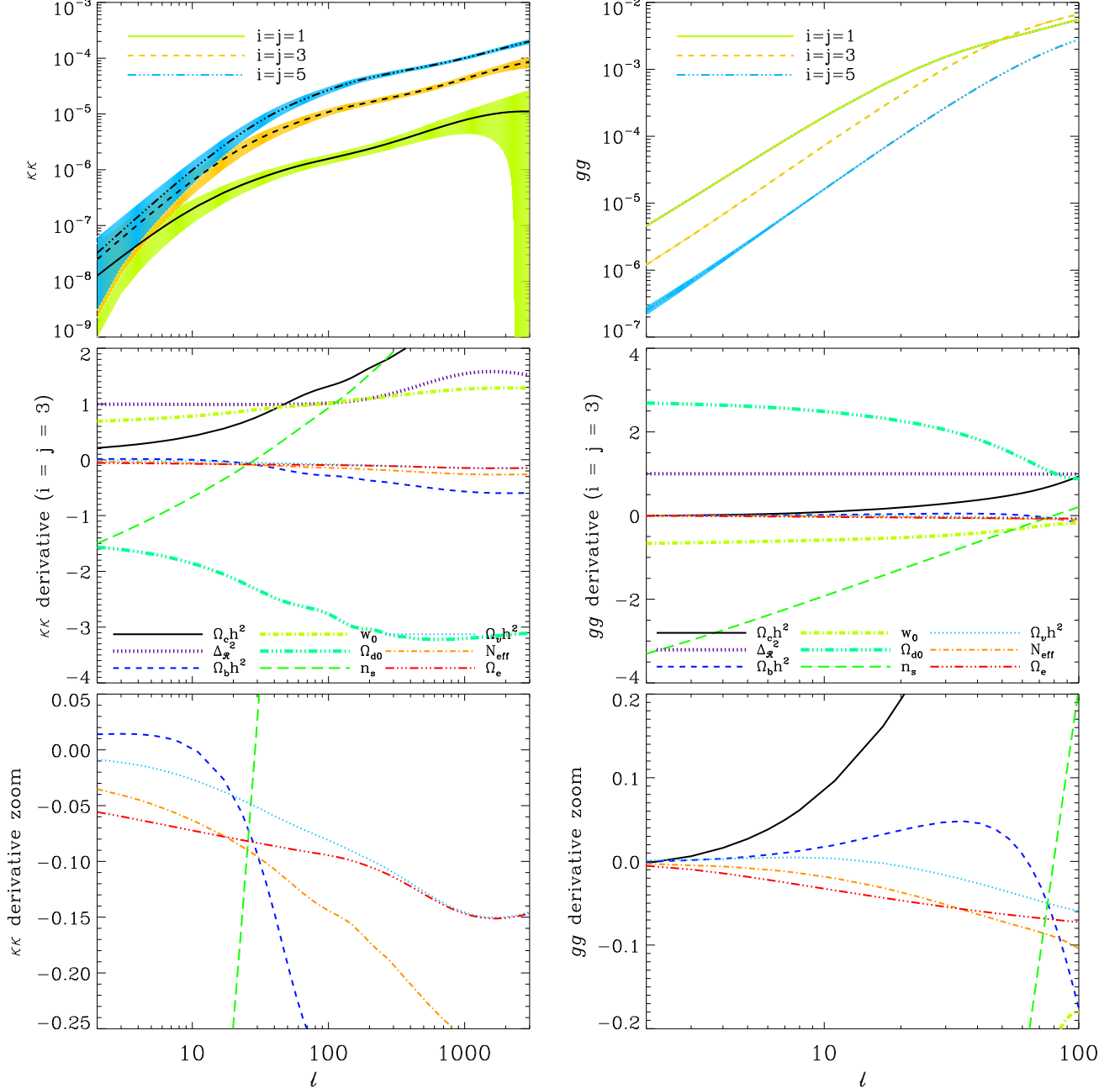


FIG. 4. *Left: Top:* Convergence power spectra $\ell(\ell+1)C_{ij}^{\kappa\kappa}/2\pi$ for the case of five tomographic bins in the fiducial cosmology. We include the expected noise for LSST as a band about the curve. *Mid:* Logarithmic derivative $d \ln C_{ij}^{\kappa\kappa}/d \ln p_k$ of the convergence power spectrum with cosmological parameters p_k for the third tomographic bin ($i=j=3$). The derivatives of the other tomographic bins have similar shapes. *Bottom:* The sub-window zooms in on the logarithmic derivatives with sum of neutrino masses (dotted blue) and EDE density (dot-dot-dashed red). *Right:* Same as *Left* but for galaxy power spectra. The noise contribution (both LSST and JDEM) is at most on sub-percent level and decreases towards smaller scales, as the noise is constant with scale whereas C_ℓ^{gg} increases with scale. This is to be contrasted with lensing tomography where $C_\ell^{\kappa\kappa}$ peaks at around $\ell=10$ and thereafter decreases continuously.

D. Galaxy Angular Power Spectrum

The galaxy-galaxy angular power spectrum $C^{gg}(\ell)$ can be obtained analogously to the derivation of $C^{\phi\phi}(\ell)$ in Eqn. 8. The two-dimensional projection of the three-dimensional biased tracer of the density

field $\delta^g(\hat{\mathbf{n}}, z)$ is

$$g_i(\hat{\mathbf{n}}) = \int_0^{z_{\max}} dz K(z) \zeta_i^g(z) \delta^g(\hat{\mathbf{n}}, z). \quad (14)$$

From $\langle g^*(\mathbf{k}, z) g(\mathbf{k}', z) \rangle = (2\pi)^3 \delta_{\mathbf{D}}(\mathbf{k} - \mathbf{k}') P_{gg}(k, z)$, we thereby obtain the projected galaxy power spectrum

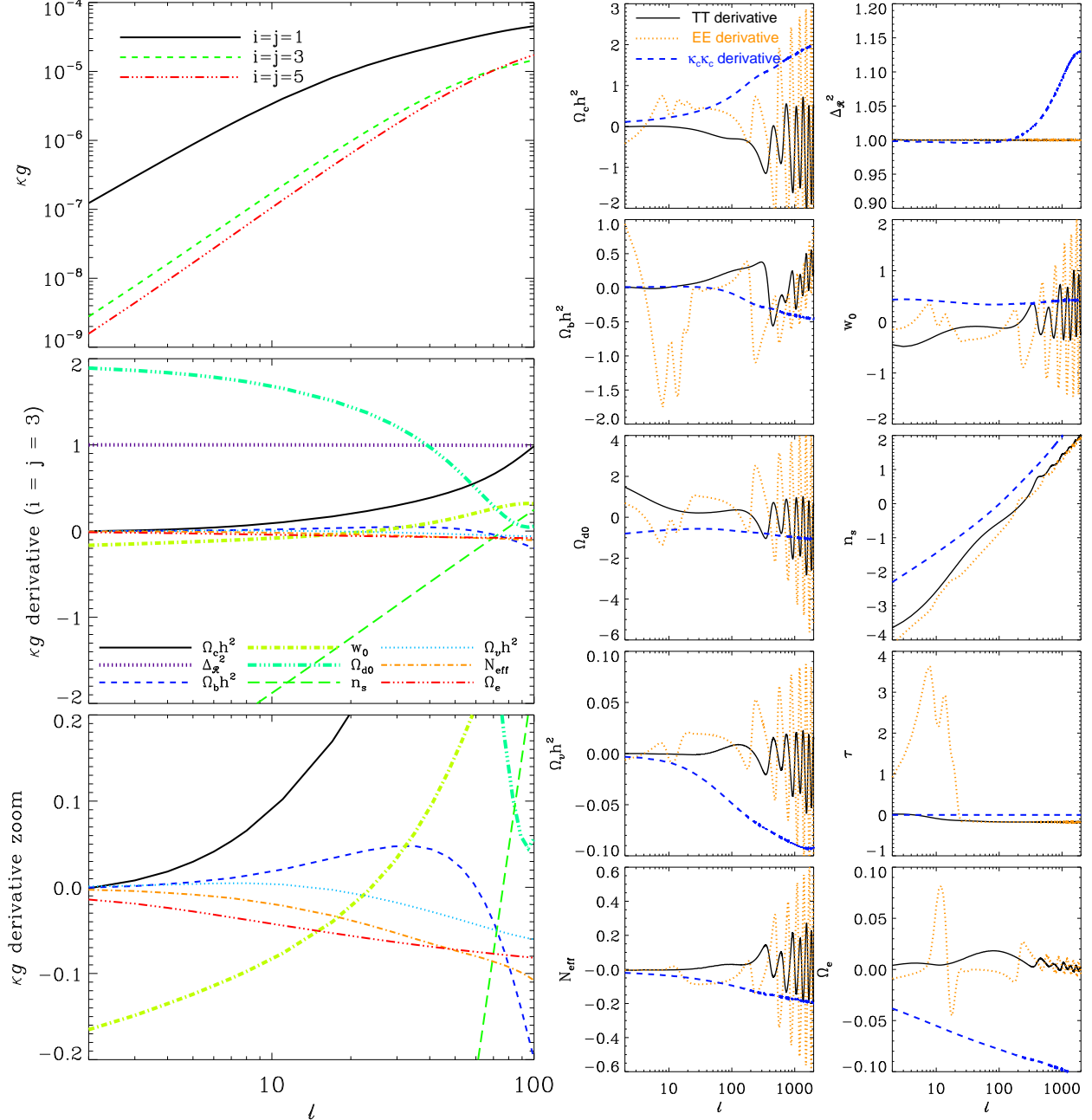


FIG. 5. *Left*: Top: Tomographic galaxy-galaxy lensing correlations $\ell(\ell+1)C_{ij}^{\kappa g}/2\pi$. Here we only illustrate a subset of cases where galaxy and lensing bins fully overlap. *Mid*: Logarithmic derivatives of the power spectra $d \ln C_{ij}^{\kappa g}/d \ln p_k$ with parameters p_k for the third tomographic bin in both galaxy and lensing (similar characteristics for other bins). *Bottom*: Zooming in on the derivatives with EDE density and sum of neutrino masses. *Right*: Logarithmic derivatives of the CMB temperature (solid black), E-mode (dashed blue), and lensing potential (dotted red) power spectra with cosmology.

in the Limber approximation:

$$C_{ij}^{gg}(\ell) = \int_0^{z_{\max}} dz K(z) \zeta_i^g(z) \zeta_j^g(z) \frac{H(z)}{\chi^2(z)} P_{gg}(k, z), \quad (15)$$

where the weights for $z_i < z < z_{i+1}$ are

$$\zeta_i^g(z) = \rho(z)/\bar{n}_i, \quad (16)$$

and $\zeta_i^g(z) = 0$ if $z \notin (z_i, z_{i+1})$. As a result, only the auto-correlations survive the integral. In the linear regime, the three-dimensional galaxy power spectrum,

$P_{gg}(k, z)$, is related to the matter power spectrum via the bias $b(k, z)$:

$$C_{ij}^{gg}(\ell) = A_\ell^{gg} \int_0^{z_{\max}} dz K(z) \zeta_i^g(z) \zeta_j^g(z) \times H(z) \chi(z) b^2(k, z) \Delta_{\delta\delta}^2 \left(\frac{\ell+1/2}{\chi(z)}, z \right), \quad (17)$$

where amplitude $A_\ell^{gg} = 2\pi^2 (\ell+1/2)^{-3}$. Restricting the analysis to largely linear scales (see Table II), we include a time-varying linear bias by the first-order

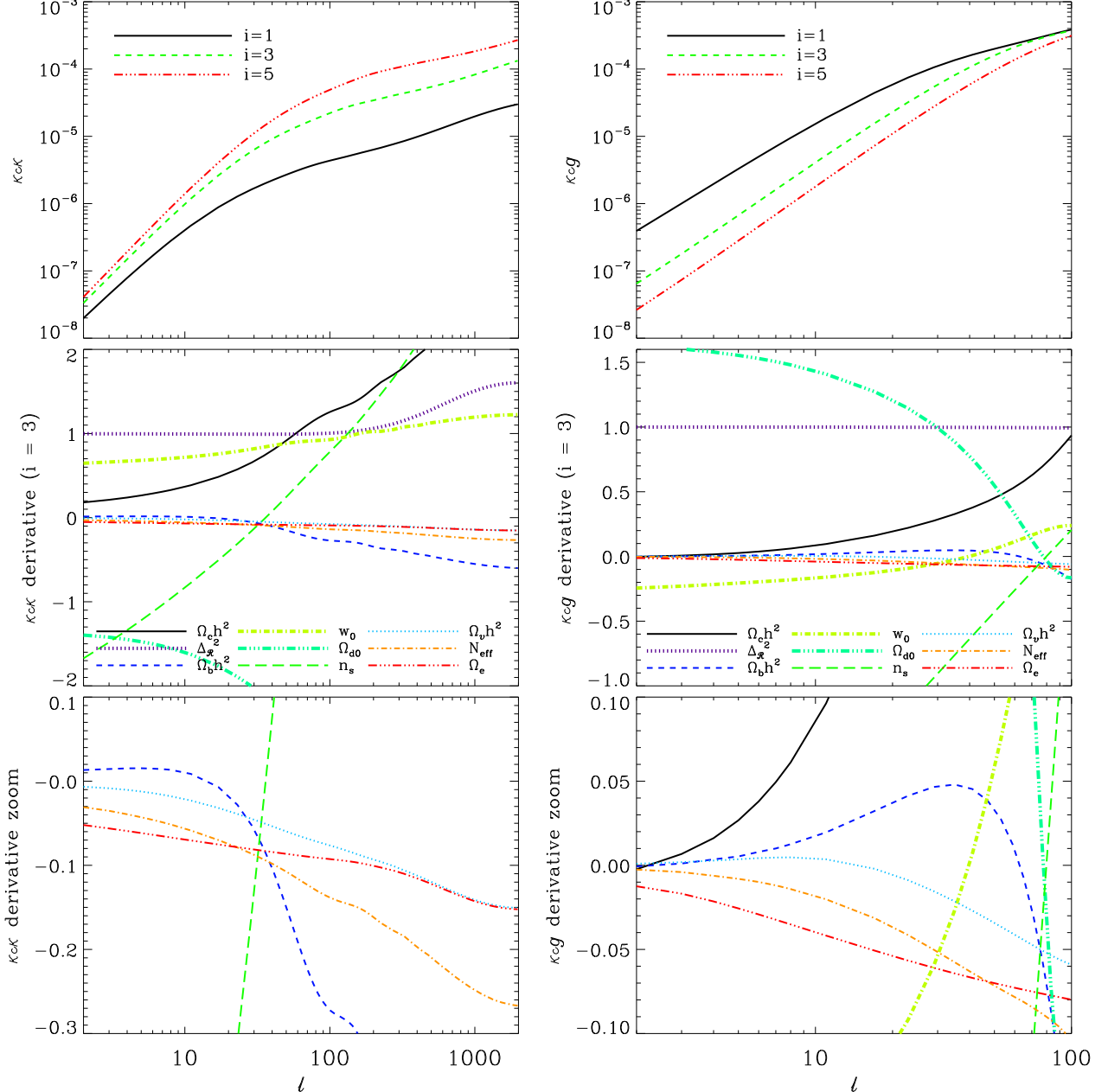


FIG. 6. *Left: Top:* Correlations between weak lensing of the CMB and low-redshift sources $\ell(\ell+1)C_i^{\kappa c \kappa}/2\pi$ for three of the five tomographic bins. *Mid:* Logarithmic derivatives of the power spectrum $d \ln C_i^{\kappa c \kappa}/d \ln p_k$ with parameters p_k for the third tomographic bin (similar characteristics for other bins). *Bottom:* Zoom on derivatives with EDE density and sum of neutrino masses. *Right:* Same as *Left* but for correlations between galaxy tomography and lensing of the CMB.

expansion $b(z) = b_0 + b_1 z$. A Gaussian prior of 10% is applied to these two bias parameters [76, 77], and the fiducial values are set to $[b_0, b_1] = [1.0, 0.8]$ [78].

E. Galaxy-Lensing Correlation

The cross-correlation of the source galaxy distribution and the weak lensing convergence is:

$$C_{ij}^{g\phi}(\ell) = \int_0^{z_{\max}} dz K(z) \zeta_i^g(z) \zeta_j^\phi(z) \frac{H(z)}{\chi^2(z)} P_{g\Phi}(k, z). \quad (18)$$

Correlations between tomographic bins where the galaxy bin lies behind the lensing bin are zero (resulting in 15 out of 25 non-zero correlations). The power spectrum of galaxy and potential perturbations may be written as:

$$P_{g\Phi}(k, z) = \frac{3}{2} \frac{\Omega_m}{a(z)} \left(\frac{H_0}{k} \right)^2 b(k, z) r_c(k, z) P_{\delta\delta}(k, z), \quad (19)$$

where we have introduced the correlation coefficient r_c defined through the relation $P_{g\delta}^2(k, z) = r_c^2(k, z) P_{gg}(k, z) P_{\delta\delta}(k, z)$. Then, using $C_\ell^{g\kappa} = -\ell(\ell +$

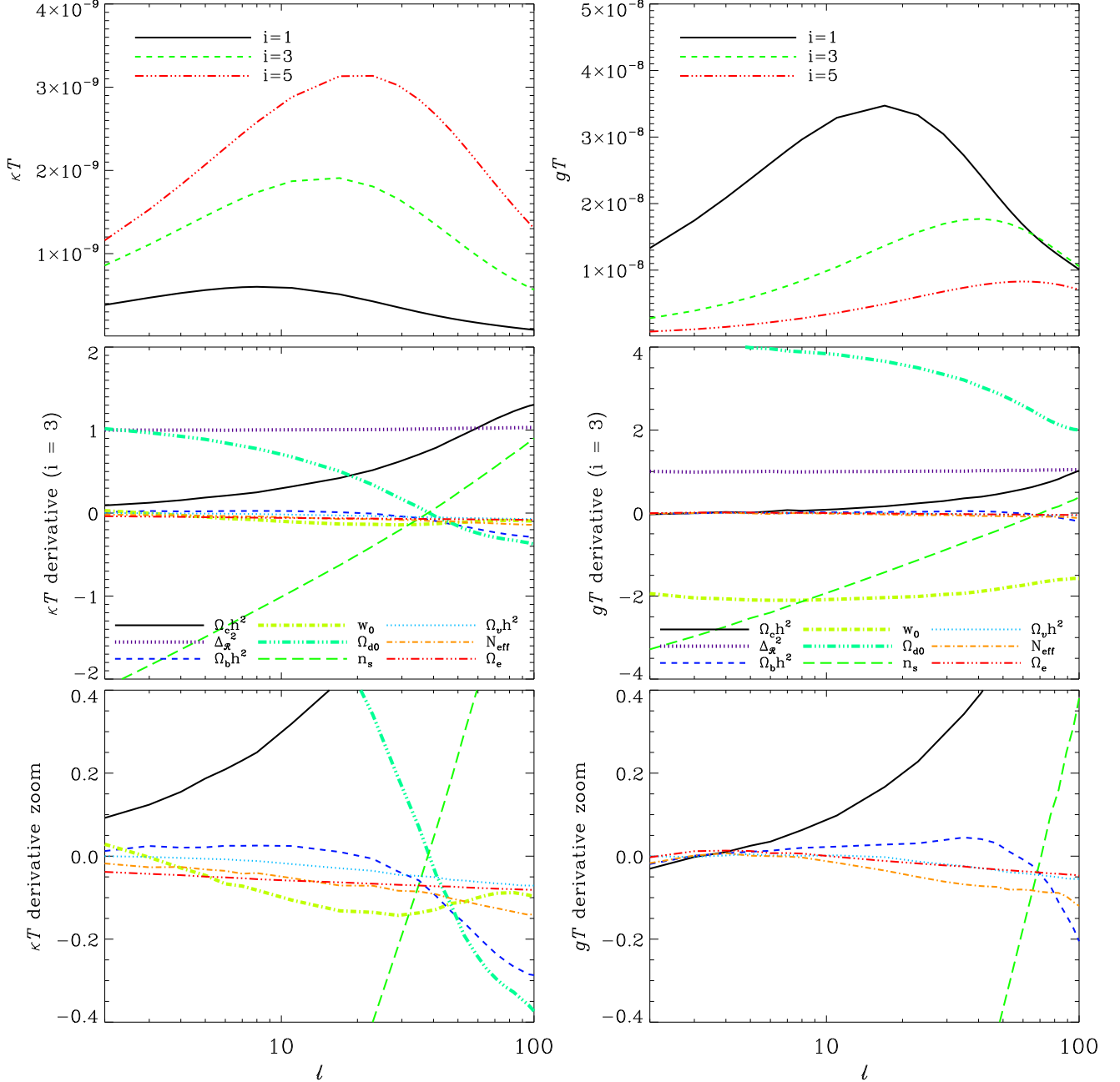


FIG. 7. *Left: Top:* ISW-WL correlations $-\ell(\ell+1)C_i^{\kappa T}/2\pi$ for three of the five tomographic bins. *Mid:* Logarithmic derivatives of the power spectrum $d \ln C_i^{\kappa T}/d \ln p_k$ with parameters p_k for the third bin (similar characteristics for other bins). *Bottom:* Zoom on the EDE and neutrino mass derivatives. *Right:* Same as *Left* but for ISW-galaxy correlations.

1) $C_\ell^{g\phi}/2$, we may write the angular power spectrum for galaxy and weak lensing correlation as:

$$C_{ij}^{g\kappa}(\ell) = A_\ell^{g\kappa} \int_0^{z_{\max}} dz K(z) \zeta_i^g(z) \zeta_j^\kappa(z) \times \quad (20)$$

$$(1+z)H(z)\chi^3(z)b(k,z)r_c(k,z)\Delta_{\delta\delta}^2\left(\frac{\ell+1/2}{\chi(z)}, z\right),$$

where we have defined $A_\ell^{g\kappa} = -(3\pi^2/2)(\Omega_m H_0^2)\ell(\ell+1)(\ell+1/2)^{-5}$. Restricting the analysis to linear scales, we fix $r_c \equiv 1$ in our calculations.

F. Cosmic Microwave Background (T , E , κ_c)

We consider CMB information from the temperature field (T), E-mode polarization (E), and weak lensing of the CMB (κ_c). The temperature and E-mode polarization power spectra (and their cross-correlation) are obtained from a modified version of the Boltzmann code CAMB [79].

As for lensing of the CMB photons [68, 80, 81] (also see Refs. [82, 83] for detections of the lensing power spectrum), we calculate it in the same manner as in

Eqn. 13 with the source constrained to be at the redshift of decoupling (z_{dec}), such that

$$\zeta^{\kappa_c}(z) = \frac{-2}{H(z)\chi(z)} \frac{\chi(x(z_{\text{dec}}) - x(z))}{\chi(z_{\text{dec}})}. \quad (21)$$

Hence, aside from $\zeta_i^\kappa(z)\zeta_j^\kappa(z) \rightarrow \zeta^{\kappa_c}(z)\zeta^{\kappa_c}(z)$ (and $z_{\text{max}} = z_{\text{dec}}$), $C^{\kappa_c\kappa_c}(\ell)$ has the same functional form as $C_{ij}^{\kappa\kappa}(\ell)$. Similarly, the cross-correlation spectrum $C_i^{\kappa\kappa_c}(\ell)$ has the same form as $C_{ij}^{\kappa\kappa}(\ell)$ with the substitution $\zeta_j^\kappa(z) \rightarrow \zeta^{\kappa_c}(z)$, and we obtain $C_i^{g\kappa_c}(\ell)$ by replacing $\zeta_j^\kappa(z)$ with $\zeta^{\kappa_c}(z)$ in $C_{ij}^{g\kappa}(\ell)$.

In Figure 5 we show the logarithmic derivatives of the CMB temperature, E-mode, and lensing potential power spectra with cosmological parameters. In particular, it is evident that both CMB temperature and lensing measurements of the early and late universe are necessary to break the degeneracies between early dark energy and sum of neutrino masses.

G. ISW-Lensing Correlation

We consider five distinct lensing cross-correlations: the first is that of weak lensing in redshift bins (i) with the lensing of the CMB photons, $C_i^{\kappa\kappa_c}(\ell)$; the second is that of galaxy counts in redshift bins (i) with the lensing of the CMB photons, $C_i^{g\kappa_c}(\ell)$; the third is that of galaxy counts in redshift bins (i) with weak lensing in redshift bins (j), $C_{ij}^{g\kappa}(\ell)$; the fourth is that of weak lensing in redshift bins (i) with the unlensed temperature, $C_i^{\kappa T}(\ell)$; and the fifth is that of lensing of CMB photons with the unlensed temperature, $C^{\kappa_c T}(\ell)$. Having already described the first three correlations, we here discuss the last two correlations that arise due to the Integrated Sachs Wolfe (ISW) effect [84–87].

The perturbations in the CMB temperature due to the late-time gravitational redshifting of the photons is encapsulated in [72]

$$\frac{\Delta T^{\text{ISW}}(\hat{\mathbf{n}})}{T} = \int_0^{z_{\text{ls}}} dz K(z) \zeta^T(z) \dot{\Phi}(\hat{\mathbf{n}}, z), \quad (22)$$

where the overdot denotes a derivative with time t , and the ISW weight is

$$\zeta^T(z) = \frac{2}{(1+z)H(z)}. \quad (23)$$

The cross spectrum of the respective Fourier coefficients is given by

$$\frac{1}{T} \langle \phi_i^*(\mathbf{l}) \Delta T(\mathbf{l}') \rangle = (2\pi)^2 \delta_{\text{D}}(\mathbf{l} - \mathbf{l}') C_i^{\phi T}(\ell), \quad (24)$$

which via the Limber approximation reduces to

$$C_i^{\phi T}(\ell) = \int_0^{z_{\text{max}}} dz K(z) \zeta_i^\kappa(z) \zeta^T(z) \frac{H(z)}{\chi^2(z)} P_{\Phi\dot{\Phi}}(k, z). \quad (25)$$

To find $P_{\Phi\dot{\Phi}}(k, z)$, the time derivative of the potential

$$\dot{\Phi}(\mathbf{k}, z) = \frac{3}{2} \frac{\Omega_m}{(1+z)^{-1}} \left(\frac{H_0}{k} \right)^2 \left(\frac{\delta(\mathbf{k}, z)}{H^{-1}(z)} - \dot{\delta}(\mathbf{k}, z) \right), \quad (26)$$

and hence

$$P_{\Phi\dot{\Phi}}(k, z) = \frac{9}{4} \frac{\Omega_m^2}{(1+z)^{-2}} \left(\frac{H_0}{k} \right)^4 \left(P_{\delta\dot{\delta}} - \frac{P_{\delta\delta}}{H^{-1}(z)} \right). \quad (27)$$

To compute $P_{\delta\dot{\delta}}$, we note that in the linear regime $P_{\delta\dot{\delta}} = \frac{1}{2} \frac{\partial}{\partial t} P_{\delta\delta}$. This relation has been numerically verified to hold in the nonlinear regime up to $\ell = 5000$ [88]. Hence, we adopt this relation so that

$$P_{\Phi\dot{\Phi}}(k, z) = -\frac{9}{4} \frac{\Omega_m^2 H(z)}{(1+z)^{-2}} \left(\frac{H_0}{k} \right)^4 \left(1 + \frac{1+z}{2} \frac{\partial}{\partial z} \right) P_{\delta\delta}, \quad (28)$$

and the resulting $\kappa - T$ angular power spectrum is then given by

$$C_i^{\kappa T}(\ell) = A_\ell^{\kappa T} \int_0^{z_{\text{max}}} dz K(z) \zeta_i^\kappa(z) \zeta^T(z) \chi^5(z) \times (29) \\ (1+z)^2 H^2(z) \left(1 + \frac{1+z}{2} \frac{\partial}{\partial z} \right) \Delta_{\delta\delta}^2 \left(\frac{\ell + 1/2}{\chi(z)}, z \right),$$

where the amplitude $A_\ell^{\kappa T} = (\ell(\ell+1)/2)^{-1} A_\ell^{\kappa\kappa} = (9\pi^2/4) (\Omega_m H_0^2)^2 \ell(\ell+1)(\ell+1/2)^{-7}$. As the derivative $|\frac{1+z}{2} \frac{\partial}{\partial z} \Delta_{\delta\delta}^2| < \Delta_{\delta\delta}^2$, and the lensing weight contains a negative sign, it follows that $C_i^{\kappa T}(\ell) < 0$. We obtain $C^{\kappa_c T}(\ell)$ by replacing $\zeta_i^\kappa(z)$ with $\zeta^{\kappa_c}(z)$ in the above equation.

H. ISW-Galaxy Correlation

To obtain the ISW-galaxy correlation,

$$C_i^{gT}(\ell) = \int_0^{z_{\text{max}}} dz K(z) \zeta_i^g(z) \zeta^T(z) \frac{H(z)}{\chi^2(z)} P_{g\dot{\Phi}}(k, z), \quad (30)$$

we follow the same steps as for the ISW-lensing correlation and obtain

$$P_{g\dot{\Phi}}(k, z) = \frac{3}{2} \frac{\Omega_m}{a(z)} \left(\frac{H_0}{k} \right)^2 b(k, z) r_c(k, z) \quad (31) \\ \times (H(z) P_{\delta\delta}(k, z) - P_{\delta\dot{\delta}}(k, z)).$$

We thereby find the projected spectrum

$$C_i^{gT}(\ell) = A_\ell^{gT} \int_0^{z_{\text{max}}} dz K(z) \zeta_i^g(z) \zeta^T(z) \quad (32) \\ \times (1+z) H^2(z) \chi^3(z) b(k, z) r_c(k, z) \\ \times \left(1 + \frac{1+z}{2} \frac{\partial}{\partial z} \right) \Delta_{\delta\delta}^2 \left(\frac{\ell + 1/2}{\chi(z)}, z \right),$$

where amplitude $A_\ell^{gT} = -3\pi^2 (\Omega_m H_0^2) (\ell + 1/2)^{-5}$.

I. Supernovae

We include the supernovae distances in our analysis for their ability to constrain the expansion history of the low-redshift universe [89]. The observable quantity is the apparent magnitude:

$$m = 5 \log_{10} \left(\frac{(1+z)\chi(z)}{\text{Mpc}} \right) + 25 + M, \quad (33)$$

where M is the absolute magnitude, and we marginalize over it around the fiducial value of $M_{\text{fid}} = -19.3$ with a Gaussian prior of 0.6. This is equivalent to treating the distance modulus $\mu(z) = m(z) - M$ as the observable, and adding to that the nuisance parameter \mathcal{M} . The fisher matrix of the prospective supernova measurements is then

$$F_{\alpha\beta}^{\text{SN}} = \frac{1}{\sigma_m^2} \int_0^{z_{\text{max}}} dz N(z) \frac{\partial m}{\partial p_\alpha} \frac{\partial m}{\partial p_\beta}, \quad (34)$$

where σ_m is the measurement uncertainty, $N(z)$ is the redshift distribution of the SNe, z_{max} is the redshift of the farthest SN, and p represents the cosmological parameters.

Although, we do not expect a strong measurement of EDE from SNe, we will see that it does help in breaking some of the degeneracies in the parameters of the background cosmology, in particular the dark energy at the present epoch. To this end, we uniformly distribute a set of 300 SNe at $z < 0.1$ [66, 90]. For the space-based JDEM survey, we add 2000 SNe in the range $0.1 < z < 1.7$ [91], whereas for the LSST survey we distribute 3.0×10^5 SNe (corresponding to six years of data) between $0.1 < z < 0.8$ [92]. For each supernova we take the intrinsic noise to be Gaussian in magnitude with $\sigma_{\text{int}} = 0.1$ [93]. We divide the Hubble diagram for $z > 0.1$ into 50 redshift bins, and associate each bin with a redshift-dependent systematic error floor of magnitude

$$\delta_m(z) = 0.01(0.1/\Delta z)^{1/2}(1.7/z_{\text{max}})(1+z)/2.7, \quad (35)$$

where Δz is the width of the relevant redshift bin [94]. For the ground-based LSST survey, we allow for photometric uncertainties of the form

$$\sigma_z = \frac{\sigma_F(1+z)}{\sqrt{N_c}}, \quad (36)$$

where $N_c = 100$ is the number of spectra used in the photo- z calibration in each bin, and $\sigma_F = 0.01$. Assuming no correlation between bins, the total magnitude uncertainty is thereby quantified via

$$\sigma_m(z) = \sqrt{\frac{1}{N_{\text{bin}}}\sigma_{\text{int}}^2 + \left(\frac{\partial m}{\partial z}\right)^2 \sigma_z^2 + \delta_m^2(z)}, \quad (37)$$

where N_{bin} is the number of SNe in each redshift bin, and $\sigma_z = 0$ for the spectroscopic JDEM survey. The

dominant contribution to the total error comes from the systematic floor, and the photometric redshift errors turn significant only for more pessimistic choices of σ_F .

For a fixed z_{max} , the SN constraints on the underlying cosmology are robust to variations in the particular SN redshift distribution of the survey, while this maximum redshift itself imposes an important limiting factor on the cosmological constraints [94–97]. Due to the systematic floor, we find the LSST constraints on the underlying cosmology from SNe remain effectively unchanged after the first year’s data. The existence of a systematic floor combined with SNe extending to higher redshifts explain why our JDEM configuration provides stronger constraints than our LSST configuration when it comes to SN explorations of dark energy (as shown in Table IV).

III. RESULTS

We next explore the constraints on early dark energy from future weak lensing, large-scale structure, SN, and CMB measurements (and all relevant cross-correlations). We begin by listing the observational properties of these probes. Then we elaborate on the constraints on the underlying cosmology of the universe, and the biases in the cosmological parameters that arise due to a potential neglect of early dark energy.

A. Survey Properties

We consider Planck [98, 99] for CMB temperature, polarization, and lensing measurements, and compare this to a future mid-cost CMBPol [100, 101] mission (Epic-2m). For the large-scale structure, weak lensing, and SN observations, we compare two generic types of surveys: 1) a ”wide” survey, and 2) a ”deep” survey.

For the ”wide” configuration, we consider a survey covering half of the sky, such as the ground-based Large Synoptic Survey Telescope (LSST) [102, 103]. For comparison, for the ”deep” configuration, we consider a survey covering a tenth of the sky, such as a space-based Joint Dark Energy Mission (JDEM) candidate like the SuperNova Acceleration Probe (SNAP) [91, 104–106]. For weak lensing and galaxy clustering measurements, beyond the sky coverage, we only allow for the number density of source galaxies to be different between these two survey configurations (as seen in Table I). For the SNe, the two survey configurations are different in the number and redshift extent of observations (as seen in Sec. III). We refer to the wide survey as LSST, and the deep survey as JDEM. Other surveys with similar characteristics include WFIRST [107, 108] and Euclid [109, 110].

The distribution of source galaxies is divided into five tomographic redshift bins, as the gain in cosmo-

| LARGE-SCALE STRUCTURE SURVEY PROPERTIES | | | | | | |
|---|------------------|-------------------------------|-------------------|---------------------------------|---------------------|----------|
| Probe | f_{sky} | \bar{n}_g (arcmin $^{-2}$) | z_{peak} | $\sqrt{\langle\gamma^2\rangle}$ | ℓ_{max} | No. bins |
| LSST | 0.5 | 50 | 1.0 | 0.22 | 3000 | 5 |
| JDEM | 0.1 | 100 | 1.0 | 0.22 | 3000 | 5 |
| LSST ₁₀₀₀ | 0.5 | 50 | 1.0 | 0.22 | 1000 | 5 |
| JDEM ₁₀₀₀ | 0.1 | 100 | 1.0 | 0.22 | 1000 | 5 |

TABLE I. Description of the ground-based (LSST) and space-based (JDEM) probes. The redshift bins of the source distribution are delimited at [0.75, 1.1, 1.45, 1.95, 3.0], such that each tomographic bin contains roughly the same number density of galaxies. The minimum angular multipole $\ell_{\text{min}} = 2$ (see text for more details).

logical information diminishes rapidly for more than five bins [49, 67]. The number density of sources in a square arcminute in each redshift bin (with boundaries $z_i < z_s < z_{i+1}$) is defined by

$$\bar{n}_i = \int_{z_i}^{z_{i+1}} dz_s \rho(z_s), \quad (38)$$

where the redshift distribution of source galaxies is taken to be of the form [57]:

$$\rho(z_s) = \bar{n}_g \frac{z_s^\alpha}{2z_0^3} e^{-(z_s/z_0)^\beta}. \quad (39)$$

We adopt $\{z_0 = 0.5, \alpha = 2, \beta = 1\}$ [103], appropriate for LSST [102, 111], normalized such that $\int_0^\infty dz \rho(z) = \bar{n}_g$. We use the same distribution to describe our JDEM source population [91, 104, 105] with a factor of 2 higher \bar{n}_g value (see Table I).

The observed convergence power spectrum, identical to that of the shear [56], is contaminated by shot noise due to the finite source density, as well as uncertainty in the intrinsic shapes of the source galaxies, leading to

$$\tilde{C}_{ij}^{\kappa\kappa}(\ell) = \sqrt{\frac{2f_{\text{sky};\kappa}^{-1}}{2\ell+1}} (C_{ij}^{\kappa\kappa}(\ell) + \delta_{ij} \langle\gamma^2\rangle / \bar{n}_i), \quad (40)$$

which assumes that the noise is uncorrelated between tomographic bins. Similarly, for the galaxy angular power spectrum,

$$\tilde{C}_{ij}^{gg}(\ell) = \sqrt{\frac{2f_{\text{sky};g}^{-1}}{2\ell+1}} (C_{ij}^{gg}(\ell) + \delta_{ij} / \bar{n}_i). \quad (41)$$

We take the intrinsic shape uncertainty of the source galaxies to be redshift independent: $\langle\gamma^2\rangle^{1/2} = 0.22$, in accordance with expected results for the future ground-based probe. For simplicity, we keep the same source distribution and intrinsic shear uncertainty for the surveys on ground and space, modifying only the source density to twice that of the ground-based survey, and the width of the survey to a tenth of the sky. Table I summarizes the characteristics of the two surveys.

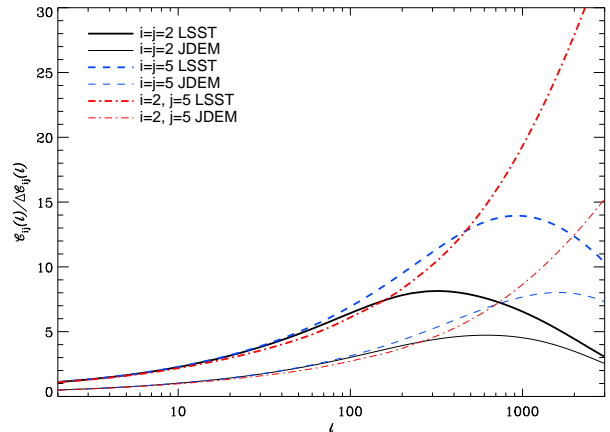


FIG. 8. Weak lensing signal-to-noise $C_{ij}^{\kappa\kappa}(\ell)/\Delta C_{ij}^{\kappa\kappa}(\ell)$ for combinations of the second and fifth tomographic bins in the fiducial cosmology, for LSST (thick) and JDEM (thin).

In Figure 4, we plot the power spectrum of the convergence for a subset of the five tomographic bins (with the redshift divisions listed in the caption of Table I). We divide the power spectrum by its noise,

$$\Delta C_{ij}^{\kappa\kappa}(\ell) = \sqrt{\left(\tilde{C}_{ii}^{\kappa\kappa}(\ell)\tilde{C}_{jj}^{\kappa\kappa}(\ell) + \tilde{C}_{ij}^{\kappa\kappa}(\ell)^2\right)}/2, \quad (42)$$

in Figure 8. Whereas cosmic variance dominates the error on large angular scales, the shot noise is dominant on small scales. The signal to noise is consistently higher for the wider LSST than it is for the deeper JDEM. The larger width of LSST gives strong signal to noise in particular at low- ℓ , while the greater depth of a JDEM-type survey makes it increasingly competitive at high- ℓ .

For the weak lensing surveys we analyze multipoles between $\ell = 2 - 3000$ in one case, and multipoles of $\ell = 2 - 1000$ as a second case. The cutoffs at $\ell = [1000, 3000]$ largely avoid non-Gaussianities of the convergence field [112–114], as well as uncertainties from baryonic physics that increase at larger multipoles [115–118]. We impose a cutoff in the matter power spectrum for $k > k_{\text{max}} = 10 h/\text{Mpc}$, which implies that for the smallest angular scales, $\ell_{\text{max}} = [1000, 3000]$, distances below $\chi = [100, 300] \text{ Mpc}/h$ (or equivalently, redshifts below $z \simeq [1/30, 1/10]$) are wiped out in the calculation of the convergence spectrum. Thus, the cutoffs ensure that scales smaller than $k = 10 h/\text{Mpc}$ in the matter power spectrum are only probed at low redshift, where the number densities of sources approach zero. Recent hydrodynamic simulations that include AGN feedback to solve the overcooling problem have shown these cutoffs may not be conservative enough unless the baryonic effects in the power spectrum are precisely modeled [117, 118].

At the other end of the spectrum, we keep all multipoles down to $\ell_{\text{min}} = 2$. We incorporate perturbations in the dark energy fluid on these scales. While a JDEM-type survey is not expected to probe scales below $\ell \sim 10$, we have checked that our extension

| NONLINEAR CUTOFFS IN GALAXY SURVEYS | | | | | |
|-------------------------------------|------|------|------|------|------|
| Bin | 1 | 2 | 3 | 4 | 5 |
| z_{median} | 0.38 | 0.93 | 1.3 | 1.7 | 2.5 |
| k_{max} | 0.11 | 0.14 | 0.17 | 0.21 | 0.29 |
| ℓ_{max} | 120 | 320 | 490 | 720 | 1200 |

TABLE II. We effectively eliminate nonlinear scales in the constraints from galaxy surveys by setting $[C_{ij}^{gg}, C_i^{gT}, C_{ij}^{g\kappa}, C_i^{g\kappa c}](\ell > \ell_{\text{max}}) = 0$. The minimum angular scale ℓ_{max} is computed via $\ell + 1/2 = k\chi$, where we let $\chi = \chi(z_{\text{median}})$ and approximate, for the considered redshifts, $k = k_{\text{max}}(z_{\text{median}}) \simeq 0.1 \times (1 + z_{\text{median}}^{3/2}/2)$ [121].

down to $\ell = 2$ does not significantly affect our results. We use the Limber approximation [74, 119] for all angular scales for computational reasons. This will lead to some errors in the constraints but this is not a significant source of concern because the Limber approximation has been shown to work better than 3% for $\ell > 20$, better than 5% for $\ell > 10$, and better than 30% even for $\ell > 2$ (see Fig. 19 of Ref. [120]). For the galaxy surveys we eliminate nearly all nonlinear scales in our analysis by setting $[C_{ij}^{gg}, C_i^{gT}, C_{ij}^{g\kappa}, C_i^{g\kappa c}](\ell > \ell_{\text{max}}) = 0$. The minimum angular scale ℓ_{max} is computed via $\ell \simeq k\chi$, where we let $\chi = \chi(z_{\text{median}})$ and approximate, for the redshifts under consideration, $k = k_{\text{max}}(z_{\text{median}}) \simeq 0.1 \times (1 + z_{\text{median}}^{3/2}/2)$ [121]. The cutoff scales are listed in Table II.

In the next section (Sec. III B) we will find, as also reported by the Dark Energy Task Force [66], weak lensing to be strongest future probe of the underlying cosmology of the universe, owing to its sensitivity to both structure formation and the universal expansion. However, the optimism associated with lensing is predicated on overcoming the vast systematic uncertainties in both measurement and in theory [48–50, 67, 69–71, 112, 115, 116, 122–132]. These systematics include dark energy corrections to the modeling of the nonlinear matter power spectrum [48–50, 131], higher order correction terms in the lensing integral (such as due to the Born approximation and lens-lens coupling [69–71]), and uncertainties of the matter power spectrum on nonlinear scales due to the strong influence of baryonic physics [115–118, 129, 130, 132]. Observational systematics include intrinsic galaxy alignments (e.g. [123–128]), photometric redshift uncertainties, shear calibration errors, and PSF anisotropies [67, 122, 126].

Furthermore, the observed ellipticities of weakly lensed galaxies are sensitive to the reduced shear, $g = \gamma/(1 - \kappa)$, where γ is the shear and κ is the convergence. In the weak lensing regime we make use of the expansion of the reduced shear to first order in the fields: $g \approx \gamma$. For future lensing surveys, it has been shown that this approximation induces a bias on the cosmological parameters at the same order as that of the parameter constraints [133, 134]. Our main motivation is to elucidate the degradation in constraints

| CMB SURVEY PROPERTIES | | | | |
|-----------------------|---------|------|--------------------------|--------------------------|
| Experiment | Channel | FWHM | $\Delta T/T \times 10^6$ | $\Delta P/T \times 10^6$ |
| Planck | 100 | 10 | 25 | 40 |
| | 143 | 7.1 | 16 | 30 |
| | 217 | 5.0 | 24 | 49 |
| EPIC-2m | 100 | 8.0 | 0.84 | 1.19 |
| | 150 | 5.0 | 0.81 | 1.15 |
| | 220 | 3.5 | 1.24 | 1.75 |

TABLE III. Experimental specifications for the Planck and mid-cost CMBPol (EPIC-2m) missions. The sky fraction $f_{\text{sky}} = 0.65$, and the angular multipoles extend from $\ell_{\text{min}} = 2$ to $\ell_{\text{max}} = 2000$. The channel frequencies are given in GHz, and the angular resolutions in arcminutes.

due to EDE and the biases in the cosmological parameters from neglect of EDE. We therefore continue with the above mentioned assumption of the shear as the lensing observable.

Intrinsic galaxy alignments reflect the reality that underlying galaxies that become lensed are not inherently circularly shaped, but possess a non-trivial intrinsic ellipticity (e.g. [123–128]). The assumption that these intrinsic ellipticities are uncorrelated with each other and the gravitational shear breaks down for high-precision measurements of weak lensing from next-generation experiments. For instance, nearby galaxies that lie in the same gravitational potential of a massive dark matter halo will experience the same tidal forces, giving rise to an intrinsic-intrinsic term [123–128]. Moreover, intrinsic-shear correlations occur for pairs of galaxies where one galaxy is correlated with the surrounding density field in the foreground, thereby contributing to the lensing distortion of the background galaxy [123–128].

While intrinsic ellipticity correlations can be controlled by downweighting close galaxy pairs from the analysis [135–137], the removal of shear-ellipticity correlations is more difficult [123–128, 138–140]. Ref. [124] has shown that the dark energy EOS may be biased by 50% if intrinsic alignments are not accounted for in next-generation weak lensing experiments. The presence of intrinsic alignments also tighten the requirements on photometric redshift uncertainties by a factor of three, regardless of the fraction of catastrophic outliers [124]. Suggested approaches to avoid these degradations include halo modeling [128] and nulling techniques [139]. Alternatively, the systematic may be self-calibrated for an extended set of observables that can correlate with the weak lensing shear and intrinsic alignment signals, such as galaxy clustering and lensing magnification [125, 140] (also see [126]).

The effects of multiplicative and additive uncertainties in the convergence (e.g. from shear miscalibration and PSF anisotropies, respectively) on the measurement of dark energy are influenced by the corresponding priors. As shown in Ref. [122] (also see Refs. [49, 114]), the cosmological parameter con-

straints are compromised for multiplicative systematics at the 1% level, and mean additive shear systematics at the 10^{-5} level. The situation is analogous for the uncertainty in the photometric redshift distribution of the sources, where the parameter constraints from lensing are either heavily influenced ($\gtrsim 1\%$ prior) or minimally influenced ($\lesssim 0.1\%$ prior) by the photometric uncertainties [49, 67, 122]. Fortunately, it has been shown that a complementary spectroscopic sample of $10^4 - 10^5$ galaxies efficiently protects against photometric redshift errors as well as catastrophic outliers [141], whereas alternative methods may even satisfy the systematic requirements from photometry alone [142, 143].

Thus, in this work, we will assume that these systematic difficulties have been largely overcome with minimal influence on the constraints by the time the data from the considered next-generation lensing probes are analyzed. At the same time, we are not incorporating further statistics that can be extracted from weak lensing, such as that included in the bispectrum [144–147], or utilizing the complementarity between measurements of shear and magnification [125, 149].

We end this section with a summary of the CMB temperature, polarization and lensing noise properties. The effective experimental noise power spectrum associated with the temperature and polarization fields is given by a summation over the number of channels,

$$N^{aa}(\ell) = \left[\sum_{i=1}^{N_{\text{chan}}} \left(\left(\frac{\Delta a}{T} \right)_i e^{l(l+1)\theta_i/16 \ln 2} \right)^{-2} \right]^{-1} \quad (43)$$

where Δa is the detector noise for $a \in (T, E)$, θ denotes the beam FWHM, and we assume $N^{TE}(\ell) = 0$. The optimal noise power spectrum of a quadratic estimator of the convergence field is given by [150, 151]

$$N^{\kappa_c \kappa_c}(\ell) = \left[\sum_{l_1 l_2} \frac{(C_{l_2}^{TT} F_{l_1 l_2} + C_{l_1}^{TT} F_{l_2 l_1})^2}{2(C_{l_1}^{TT} + N_{l_1}^{\tilde{T}\tilde{T}})(C_{l_2}^{\tilde{T}\tilde{T}} + N_{l_2}^{\tilde{T}\tilde{T}})} \right]^{-1} \times (l(l+1)/2)^2 (2l+1), \quad (44)$$

where \tilde{T} denotes the lensed temperature, and

$$F_{l_1 l_2} = \sqrt{\frac{(2l_1+1)(2l+1)(2l_2+1)}{4\pi}} \begin{pmatrix} l_1 & l & l_2 \\ 0 & 0 & 0 \end{pmatrix} \times \frac{1}{2} [l(l+1) + l_2(l_2+1) - l_1(l_1+1)], \quad (45)$$

where the quantity in brackets is the Wigner-3j symbol. Finally, we define

$$\tilde{C}^{ab}(\ell) = \sqrt{\frac{2f_{\text{sky};\text{cmb}}^{-1}}{2\ell+1}} (C^{ab}(\ell) + \delta_{ab} N^{ab}(\ell)), \quad (46)$$

where $\{a, b\} \in \{T, E, \kappa_c\}$. Values for the considered CMB experiments are given in Table III. Secondary

non-Gaussianities in the covariance from the trispectrum (due to weak lensing, the ISW effect, and the SZ effect) have been shown to degrade the Planck and EPIC parameter constraints by 20% and 30% [152, 154] respectively; however, their full account lies beyond the scope of this work.

B. Comprehensive Parameter Forecasts

In previous sections we explored the qualitative influence of EDE on the lensing, galaxy, supernova, and CMB observables, via its impact on the expansion rate and matter power spectrum. We now examine how these corrections quantitatively affect the combined constraints of the dark energy. To this end, we utilize a Fisher matrix formalism [75, 155]:

$$F_{\alpha\beta}^{\text{total}} = \sum_{\ell} \Delta\ell \times \text{Tr} \left[\tilde{C}_{\ell}^{-1} \frac{\partial \mathbf{C}_{\ell}}{\partial p_{\alpha}} \tilde{C}_{\ell}^{-1} \frac{\partial \mathbf{C}_{\ell}}{\partial p_{\beta}} \right] + F_{\alpha\beta}^{\text{SN}}, \quad (47)$$

where the decoupled SN fisher matrix is defined in Eqn. 34, and for the combined observational analysis the symmetric matrix

$$\mathbf{C}_{\ell} = \begin{pmatrix} C_{\ell}^{\{\kappa\}\{\kappa\}} & C_{\ell}^{\{\kappa\}\kappa_c} & C_{\ell}^{\{\kappa\}T} & 0 & C_{\ell}^{\{\kappa\}\{g\}} \\ C_{\ell}^{\kappa_c\{\kappa\}} & C_{\ell}^{\kappa_c\kappa_c} & C_{\ell}^{\kappa_c T} & 0 & C_{\ell}^{\kappa_c\{g\}} \\ C_{\ell}^{T\{\kappa\}} & C_{\ell}^{T\kappa_c} & C_{\ell}^{TT} & C_{\ell}^{TE} & C_{\ell}^{T\{g\}} \\ 0 & 0 & C_{\ell}^{ET} & C_{\ell}^{EE} & 0 \\ C_{\ell}^{\{g\}\{\kappa\}} & C_{\ell}^{\{g\}\kappa_c} & C_{\ell}^{\{g\}T} & 0 & C_{\ell}^{\{g\}\{g\}} \end{pmatrix}, \quad (48)$$

such that $\{\kappa\}$ consists of the spectra from five tomographic bins ($\kappa_1, \kappa_2, \kappa_3, \kappa_4, \kappa_5$) and $\{g\}$ consists of the spectra from five tomographic bins (g_1, g_2, g_3, g_4, g_5). $C_{\ell}^{\{\kappa\}\{\kappa\}}$, $C_{\ell}^{\{g\}\{g\}}$, $C_{\ell}^{\{\kappa\}\{g\}}$ are therefore 5×5 submatrices, and $C_{\ell}^{\{\kappa\}\kappa_c}$, $C_{\ell}^{\{\kappa\}T}$, $C_{\ell}^{\{g\}\kappa_c}$, $C_{\ell}^{\{g\}T}$ are 5×1 submatrices. For the terms in Eqn. 47 we carry out two-sided numerical derivatives with steps of 2% in most parameter values. We have confirmed the robustness of our results to other choices of step size.

In Tables IV–X, we illustrate prospective constraints from Planck/EPIC CMB temperature (T), E-mode polarization (E), lensing (κ_c), LSST/JDEM weak lensing tomography (κ), galaxy tomography (g), SNe (s), and their combined impact (including all relevant cross-correlations shown in Eqn. 48) on the 12 considered cosmological parameters (Ω_{d0} , Ω_e , $\Omega_c h^2$, $\Omega_b h^2$, Ω_k , $\sum m_{\nu}$, N_{eff} , w_0 , n_s , $dn_s/d \ln k$, Δ_R^2 , τ).

The contents of our tables are as follows: In Table IV and Table V we consider only a flat universe, with curvature always considered in the other tables. These tables present the separate constraints on the underlying cosmology obtained from the CMB, lensing tomography, galaxy tomography, and SNe, along with the synergies attained from a combined analysis of these probes. Table V differs from Table IV in that it fixes the early dark energy density. Table VI differs from Table IV in that it allows for variation

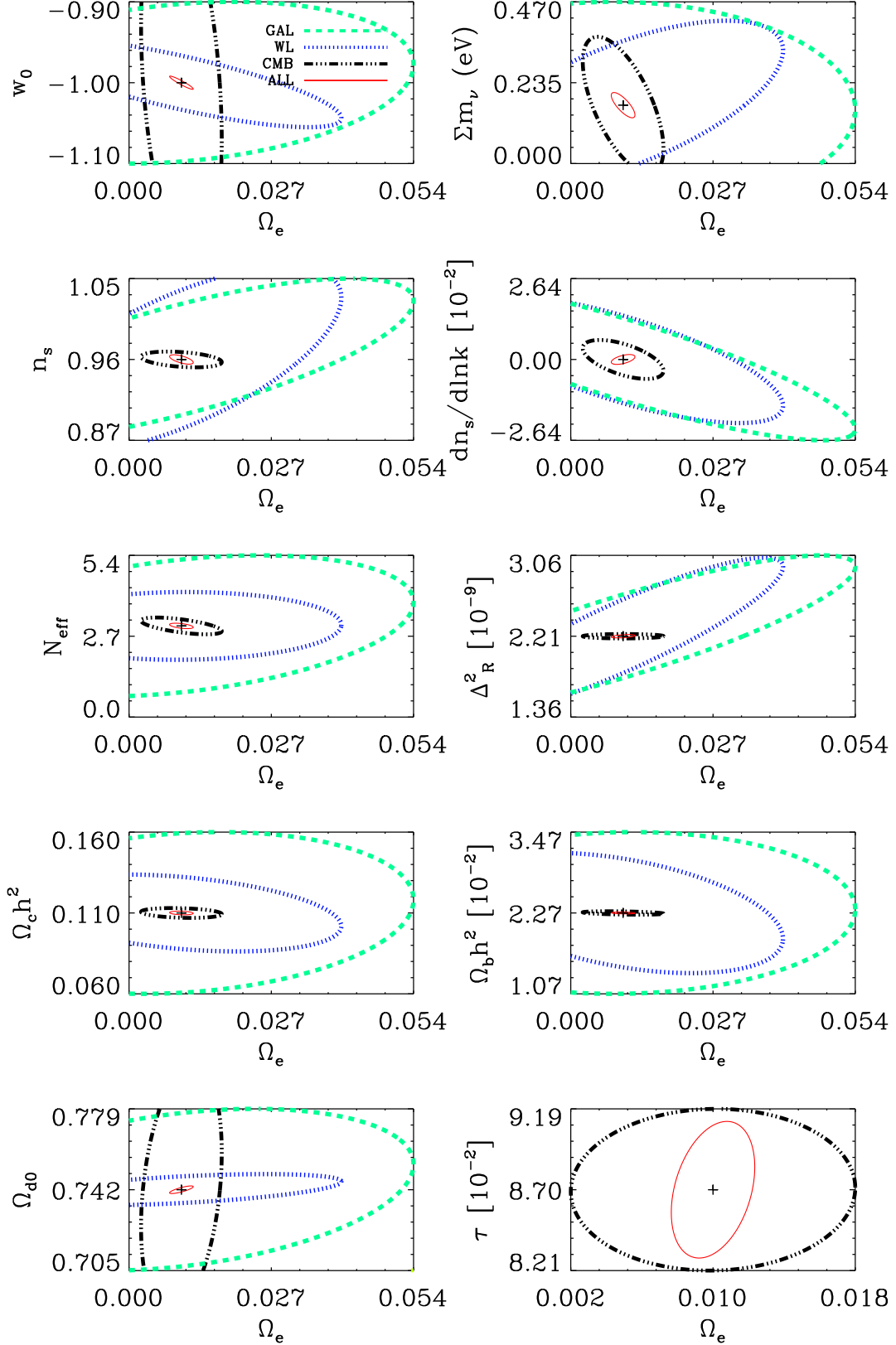


FIG. 9. Parameter degeneracies with early dark energy density (Ω_e) in a flat universe (also see Table IV) for Planck measurements of temperature and CMB lensing spectra [TT, EE, TE, $\kappa_c \kappa_c$, $\kappa_c T$] (dot-dashed, black), along with LSST tomographic weak lensing spectra [$\kappa\kappa$] (dotted, blue) and tomographic galaxy spectra [gg] (dashed, turquoise). Constraints from SNe are too weak to be visible in the shown parameter regions. The error ellipses from the combination of all these probes (including SNe), incorporating all cross-correlations (see Eqn. 48) is shown as (solid, red) curves.

in curvature. In Table X, we present results where the CMB constraints are derived from a future experiment like the proposed 2m EPIC [100, 101] (compare to Table VI). Table VII differs from Table VI in its neglect of SNe measurements. Lastly, Table IX differs from Table VI in that we neglect cross-correlations between the observables (i.e. neglecting *all* correlations between T , E , κ_c , κ , g , except for tomographic cross-correlations within κ).

We now explore each of these tables in greater detail. Table IV shows us that the dominant constraint on the fraction of dark energy at early times is drawn from the CMB (in particular TT and to some extent $T\kappa_c$) due to its deep redshift information. At a value of $\sigma(\Omega_e) = 8.6 \times 10^{-3}$ (Table IV), the Planck CMB temperature and polarization constraint is within a percent of the critical density. In general, EDE is best constrained by the CMB, followed by weak lensing tomography, galaxy tomography and SNe in that order. For comparison, the low-redshift lensing constraint from LSST on Ω_e is a factor of four (factor of six for JDEM) weaker than from the CMB. If we impose a nonlinear cutoff to the convergence spectra at $\ell_{\max} = 1000$, the situation becomes more dire, as the LSST and JDEM lensing constraints become worse by another factor of three. Similarly, the galaxy tomography constraint from LSST on Ω_e is a factor of five (factor of nine for JDEM) weaker than the CMB constraint, and the LSST SN constraint is a factor of 70 weaker (factor of 30 for JDEM) than the CMB.

Nevertheless, once the six observables (T , E , κ_c , κ , g , s) and all relevant cross-correlations (see Eqns. 47-48) from Planck (or EPIC) and LSST (or JDEM) are analyzed in a combined setting, the constraint on Ω_e improves by a factor of four over the CMB constraint. The combined constraints are equally strong regardless of the choice of LSST or JDEM for the non-CMB observations (κ , g , s). For a JDEM-like experiment, the cross-correlations improve the Ω_e constraints by a factor of about 2.

As expected, we find the late-redshift parameters more strongly constrained by the non-CMB probes. For example, in a universe where we allow for the existence of early dark energy, the LSST weak lensing constraints on the present DE density (Ω_{d0}) and EOS (w_0) of 1% and 6% are much better than the constraints obtained from just CMB lensed data of about 7% and 20% on present DE density and EOS (Table IV). Galaxy tomography measurements with LSST constrain Ω_{d0} and w_0 to 5% and 10%, respectively, whereas the strongest SN constraints are derived from JDEM, at 10% and 5% for Ω_{d0} and w_0 respectively. When we combine the probes of lensing and galaxy tomography, SNe, and CMB, the parameter constraints improve by a factor of seven in w_0 and factor of four in Ω_{d0} compared to the constraints from the strongest single probe, here weak lensing from LSST.

The results of the joint analysis don't change significantly when we relax the assumption of spatial

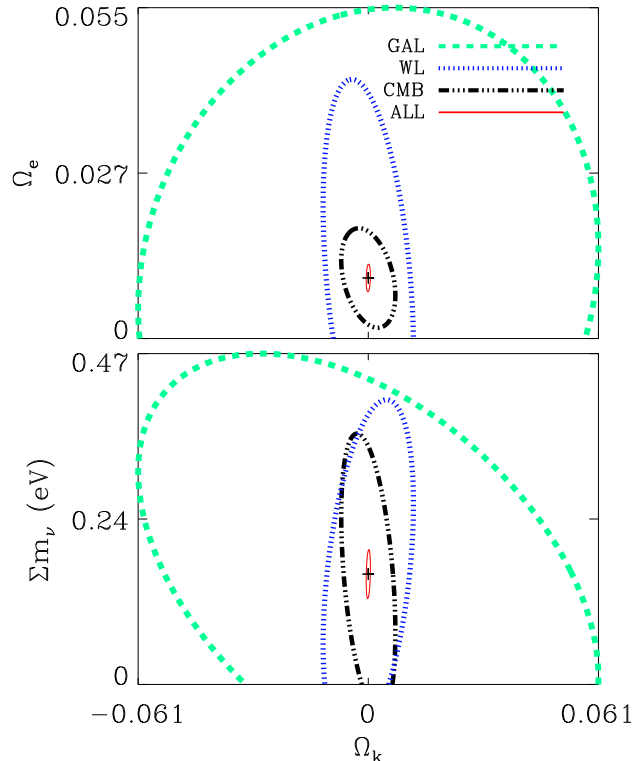


FIG. 10. Error ellipses showing degeneracies between curvature (Ω_k), early dark energy density (Ω_e) and sum of neutrino masses ($\sum m_\nu$). The curves have the same meaning as in Fig. 9. Note the strong degeneracy between curvature and sum of neutrino masses for CMB data (black, dot-dashed) that was pointed out in Ref. [152]. This degeneracy is broken when information on curvature from measures of cosmological distances are included, as shown by the solid (red) contour. The constraints in the plane of Ω_e and $\sum m_\nu$ are shown in Fig. 9.

flatness. The exception to this statement is Ω_{d0} for JDEM, which degrades by about a factor of 2 for the case where EDE density is fixed (see Table V). This is because for JDEM Ω_{d0} is most strongly constrained by SNe measurements, which require a tight bound on the curvature. In the joint analysis, the curvature density is constrained to 6×10^{-4} of the critical density, which is an order of magnitude stronger than solely with the CMB temperature and lensing. The ability to measure curvature down to this level is an exciting possibility that has been highlighted previously [156]. Our constraints on the curvature in the joint analysis, and from combining the CMB exclusively with galaxies or weak lensing in Fig. VIII, are consistent with the results in Refs. [156, 157], *even with the introduction of early dark energy*.

The sum of neutrino masses is most strongly constrained by the CMB temperature and lensing spectra (including their cross-correlation), at the level of 0.20 eV when the curvature is fixed (Table IV). When curvature is allowed to vary, the sum of neutrino mass constraint degrades to 0.22 eV. There is a strong deg-

| Probe | w_0 | Ω_{d0} | Ω_e | $\sum m_\nu(\text{eV})$ | n_s | $\frac{dn_s}{d \ln k}$ | $10^{10} \Delta_R^2$ | $\Omega_c h^2$ | $10^3 \Omega_b h^2$ | N_{eff} | τ | Ω_k |
|---|--------|---------------|------------|-------------------------|--------|------------------------|----------------------|----------------|---------------------|------------------|--------|------------|
| P | 0.42 | 0.12 | 0.0086 | 0.47 | 0.0088 | 0.0085 | 0.26 | 0.0032 | 0.27 | 0.28 | 0.0056 | — |
| PK | 0.23 | 0.057 | 0.0077 | 0.20 | 0.0085 | 0.0081 | 0.23 | 0.0031 | 0.25 | 0.28 | 0.0050 | — |
| $P_{\ell > 30} \text{K} + \sigma(\tau)$ | 0.23 | 0.060 | 0.0080 | 0.21 | 0.0085 | 0.0082 | 0.44 | 0.0031 | 0.25 | 0.28 | 0.0097 | — |
| L^κ | 0.055 | 0.0071 | 0.031 | 0.25 | 0.10 | 0.027 | 8.3 | 0.024 | 9.0 | 1.1 | — | — |
| J^κ | 0.088 | 0.012 | 0.049 | 0.38 | 0.15 | 0.040 | 13. | 0.035 | 14. | 1.7 | — | — |
| $L_{\ell < 1000}^\kappa$ | 0.072 | 0.013 | 0.081 | 0.38 | 0.17 | 0.052 | 17. | 0.049 | 16. | 1.6 | — | — |
| $J_{\ell < 1000}^\kappa$ | 0.13 | 0.024 | 0.14 | 0.67 | 0.27 | 0.088 | 28. | 0.077 | 26. | 2.5 | — | — |
| L^g | 0.099 | 0.037 | 0.044 | 0.30 | 0.087 | 0.034 | 8.5 | 0.050 | 12. | 2.4 | — | — |
| J^g | 0.21 | 0.079 | 0.078 | 0.63 | 0.16 | 0.061 | 13. | 0.11 | 26. | 5.2 | — | — |
| L^s | 0.21 | 0.27 | 0.59 | — | — | — | — | 0.16 | — | — | — | — |
| J^s | 0.045 | 0.085 | 0.27 | — | — | — | — | 0.086 | — | — | — | — |
| $\text{PKL}^\kappa \text{L}^g \text{L}^s$ | 0.0081 | 0.0017 | 0.0023 | 0.037 | 0.0050 | 0.0020 | 0.17 | 0.0011 | 0.13 | 0.090 | 0.0042 | — |
| $\text{PKJ}^\kappa \text{J}^g \text{J}^s$ | 0.0076 | 0.0014 | 0.0024 | 0.036 | 0.0052 | 0.0023 | 0.18 | 0.0012 | 0.14 | 0.088 | 0.0044 | — |
| $\text{PKL}_{\ell < 1000}^\kappa \text{L}_{\ell < 1000}^g \text{L}^s$ | 0.0084 | 0.0018 | 0.0023 | 0.039 | 0.0054 | 0.0027 | 0.18 | 0.0012 | 0.14 | 0.099 | 0.0043 | — |
| $\text{PKJ}_{\ell < 1000}^\kappa \text{J}_{\ell < 1000}^g \text{J}^s$ | 0.0078 | 0.0015 | 0.0024 | 0.037 | 0.0054 | 0.0035 | 0.19 | 0.0014 | 0.14 | 0.10 | 0.0045 | — |
| $\text{PKL}^\kappa \text{L}^g \text{L}^s + \Omega_k$ | 0.0085 | 0.0019 | 0.0023 | 0.038 | 0.0051 | 0.0021 | 0.20 | 0.0013 | 0.13 | 0.090 | 0.0044 | 0.00056 |
| $\text{PKJ}^\kappa \text{J}^g \text{J}^s + \Omega_k$ | 0.0076 | 0.0021 | 0.0025 | 0.036 | 0.0055 | 0.0024 | 0.19 | 0.0012 | 0.14 | 0.090 | 0.0045 | 0.00075 |

TABLE IV. 1σ uncertainties on cosmological parameters from a combination of probes. P denotes CMB T, E, TE modes for a Planck survey. K denotes the CMB lensing potential power spectrum and the correlation with the temperature field for Planck. L denotes an LSST type survey, whereas J denotes a JDEM type survey, and the superscripts κ, g, s , refer to weak lensing tomography, galaxy tomography, and supernova measurements, respectively. When we combine more than one probe, all relevant cross-correlations between the selected probes are included. Thus, for the case of $\text{PKL}^\kappa \text{L}^g$, all cross-correlations between $[T, E, \kappa_c, \kappa, g]$ are included (see Eqn. 48). The subscripts with $\ell < 1000$ refer to cutoffs of the respective auto-correlations (and all related cross-correlations) at $\ell = 1000$. At redshifts $z = [0, 1, 2, 3]$ the early dark energy constitutes $[0, 2.1, 8.0, 17.7]\%$ of the overall amount of dark energy (quantified as $\Omega_d(z) - \Omega_w(z)/\Omega_d(z)$ with $w = -1$ and $\Omega_e = 0.01$). For the case where $\ell < 30$ modes in CMB polarization data are excluded, we add a prior of 0.01 on the optical depth.

| Probe | w_0 | Ω_{d0} | Ω_e | $\sum m_\nu(\text{eV})$ | n_s | $\frac{dn_s}{d \ln k}$ | $10^{10} \Delta_R^2$ | $\Omega_c h^2$ | $10^3 \Omega_b h^2$ | N_{eff} | τ | Ω_k |
|--|--------|---------------|------------|-------------------------|--------|------------------------|----------------------|----------------|---------------------|------------------|--------|------------|
| $\text{P} - \Omega_e$ | 0.42 | 0.11 | — | 0.46 | 0.0086 | 0.0072 | 0.26 | 0.0032 | 0.25 | 0.24 | 0.0055 | — |
| $\text{PK} - \Omega_e$ | 0.21 | 0.055 | — | 0.15 | 0.0079 | 0.0066 | 0.23 | 0.0030 | 0.23 | 0.22 | 0.0050 | — |
| $\text{P}_{\ell > 30} \text{K} - \Omega_e + \sigma(\tau)$ | 0.22 | 0.058 | — | 0.17 | 0.0079 | 0.0066 | 0.44 | 0.0030 | 0.23 | 0.22 | 0.0097 | — |
| $L^\kappa - \Omega_e$ | 0.033 | 0.0061 | — | 0.19 | 0.075 | 0.018 | 3.9 | 0.023 | 8.1 | 1.1 | — | — |
| $J^\kappa - \Omega_e$ | 0.053 | 0.0097 | — | 0.30 | 0.12 | 0.029 | 6.1 | 0.034 | 13. | 1.7 | — | — |
| $L_{\ell < 1000}^\kappa - \Omega_e$ | 0.050 | 0.0075 | — | 0.37 | 0.13 | 0.025 | 6.7 | 0.049 | 16. | 1.5 | — | — |
| $J_{\ell < 1000}^\kappa - \Omega_e$ | 0.083 | 0.013 | — | 0.65 | 0.22 | 0.044 | 12. | 0.076 | 26. | 2.4 | — | — |
| $L^g - \Omega_e$ | 0.096 | 0.035 | — | 0.30 | 0.060 | 0.017 | 4.4 | 0.050 | 12. | 2.2 | — | — |
| $J^g - \Omega_e$ | 0.21 | 0.067 | — | 0.60 | 0.13 | 0.038 | 8.0 | 0.11 | 26. | 4.7 | — | — |
| $L^s - \Omega_e$ | 0.13 | 0.057 | — | — | — | — | — | 0.080 | — | — | — | — |
| $J^s - \Omega_e$ | 0.042 | 0.012 | — | — | — | — | — | 0.075 | — | — | — | — |
| $\text{PKL}^\kappa \text{L}^g \text{L}^s - \Omega_e$ | 0.0026 | 0.0010 | — | 0.023 | 0.0039 | 0.0017 | 0.16 | 0.0011 | 0.13 | 0.078 | 0.0040 | — |
| $\text{PKJ}^\kappa \text{J}^g \text{J}^s - \Omega_e$ | 0.0031 | 0.00092 | — | 0.023 | 0.0047 | 0.0023 | 0.17 | 0.0012 | 0.13 | 0.084 | 0.0044 | — |
| $\text{PKL}_{\ell < 1000}^\kappa \text{L}_{\ell < 1000}^g \text{L}^s - \Omega_e$ | 0.0028 | 0.0012 | — | 0.024 | 0.0041 | 0.0025 | 0.16 | 0.0012 | 0.13 | 0.084 | 0.0041 | — |
| $\text{PKJ}_{\ell < 1000}^\kappa \text{J}_{\ell < 1000}^g \text{J}^s - \Omega_e$ | 0.0034 | 0.00099 | — | 0.023 | 0.0050 | 0.0035 | 0.17 | 0.0014 | 0.14 | 0.098 | 0.0044 | — |
| $\text{PKL}^\kappa \text{L}^g \text{L}^s + \Omega_k - \Omega_e$ | 0.0029 | 0.0014 | — | 0.028 | 0.0039 | 0.0019 | 0.18 | 0.0012 | 0.13 | 0.079 | 0.0041 | 0.00055 |
| $\text{PKJ}^\kappa \text{J}^g \text{J}^s + \Omega_k - \Omega_e$ | 0.0037 | 0.0020 | — | 0.025 | 0.0049 | 0.0023 | 0.18 | 0.0012 | 0.14 | 0.085 | 0.0044 | 0.00072 |

TABLE V. Same as Table IV (Planck CMB), for an EDE fiducial cosmology with $\Omega_e = 0.01$ kept fixed.

generacy between sum of neutrino masses and curvature as pointed out in Ref. [152], and this is evident in the bottom panel of Fig. 10. However, in the joint analysis the constraint on curvature (of 6×10^{-4} of the present critical density) is strong enough to break

this degeneracy, which will allow for an exquisite measurement of the sum of neutrino masses. Our forecasts including CMB lensing, weak lensing tomography, galaxy tomography, and supernovae show that constraints on the sum of neutrino masses at the level

| Probe | w_0 | Ω_{d0} | Ω_e | $\sum m_\nu(\text{eV})$ | n_s | $\frac{dn_s}{d \ln k}$ | $10^{10} \Delta_R^2$ | $\Omega_c h^2$ | $10^3 \Omega_b h^2$ | N_{eff} | τ | Ω_k |
|--|--------|---------------|------------|-------------------------|--------|------------------------|----------------------|----------------|---------------------|------------------|--------|------------|
| P + Ω_k | 0.43 | 0.12 | 0.0087 | 0.53 | 0.0090 | 0.0085 | 0.26 | 0.0032 | 0.27 | 0.29 | 0.0056 | 0.013 |
| PK + Ω_k | 0.26 | 0.089 | 0.0082 | 0.22 | 0.0085 | 0.0081 | 0.24 | 0.0031 | 0.26 | 0.28 | 0.0053 | 0.0073 |
| $P_{\ell > 30\text{K}} + \Omega_k + \sigma(\tau)$ | 0.27 | 0.092 | 0.0085 | 0.24 | 0.0085 | 0.0082 | 0.44 | 0.0031 | 0.26 | 0.28 | 0.0097 | 0.0075 |
| $L^\kappa + \Omega_k$ | 0.055 | 0.014 | 0.033 | 0.27 | 0.11 | 0.029 | 8.3 | 0.025 | 9.3 | 1.2 | — | 0.012 |
| $J^\kappa + \Omega_k$ | 0.089 | 0.025 | 0.055 | 0.42 | 0.16 | 0.045 | 13. | 0.037 | 14. | 1.8 | — | 0.020 |
| $L_{\ell < 1000}^\kappa + \Omega_k$ | 0.073 | 0.018 | 0.083 | 0.41 | 0.18 | 0.062 | 18. | 0.050 | 16. | 1.8 | — | 0.019 |
| $J_{\ell < 1000}^\kappa + \Omega_k$ | 0.13 | 0.033 | 0.14 | 0.70 | 0.29 | 0.10 | 30. | 0.077 | 26. | 2.8 | — | 0.032 |
| $L^g + \Omega_k$ | 0.20 | 0.040 | 0.045 | 0.34 | 0.093 | 0.035 | 8.5 | 0.053 | 12. | 3.0 | — | 0.061 |
| $J^g + \Omega_k$ | 0.39 | 0.088 | 0.087 | 0.67 | 0.20 | 0.073 | 15. | 0.12 | 27. | 6.4 | — | 0.12 |
| $L^s + \Omega_k$ | 0.21 | 0.27 | 0.59 | — | — | — | — | 0.16 | — | — | — | 0.013 |
| $J^s + \Omega_k$ | 0.046 | 0.086 | 0.27 | — | — | — | — | 0.086 | — | — | — | 0.013 |
| PKL $^\kappa$ L g L $^s + \Omega_k$ | 0.0085 | 0.0019 | 0.0023 | 0.038 | 0.0051 | 0.0021 | 0.20 | 0.0013 | 0.13 | 0.090 | 0.0044 | 0.00056 |
| PKJ $^\kappa$ J g J $^s + \Omega_k$ | 0.0076 | 0.0021 | 0.0025 | 0.036 | 0.0055 | 0.0024 | 0.19 | 0.0012 | 0.14 | 0.090 | 0.0045 | 0.00075 |
| PKL $_{\ell < 1000}^\kappa$ L $_{\ell < 1000}^g$ L $^s + \Omega_k$ | 0.0090 | 0.0022 | 0.0024 | 0.040 | 0.0054 | 0.0031 | 0.21 | 0.0013 | 0.14 | 0.10 | 0.0044 | 0.00068 |
| PKJ $_{\ell < 1000}^\kappa$ J $_{\ell < 1000}^g$ J $^s + \Omega_k$ | 0.0078 | 0.0023 | 0.0025 | 0.037 | 0.0059 | 0.0035 | 0.20 | 0.0014 | 0.15 | 0.11 | 0.0045 | 0.00081 |

TABLE VI. Same as Table IV (Planck CMB), allowing for Ω_k to vary. We include a CMB prior on the curvature for the SN surveys. For the galaxy measurements alone, the bias parameters defined in Sec. IID as $b(z) = b_0 + b_1 z$ are constrained to $\sigma\{b_0, b_1\} = \{0.16, 0.19\}$ for LSST and $\sigma\{b_0, b_1\} = \{0.34, 0.43\}$ for JDEM. Our 10% prior on these bias parameters (i.e. $\sigma\{b_0, b_1\} = \{0.1, 0.08\}$) therefore improves the constraints on cosmology. When all probes are combined, the bias parameters are constrained to $\sigma\{b_0, b_1\} = \{6.7, 3.5\} \times 10^{-3}$ for LSST and $\sigma\{b_0, b_1\} = \{7.4, 4.6\} \times 10^{-3}$ for JDEM. An imposed 10% prior is therefore rendered negligible in the multi-probe scenario.

| Probe | w_0 | Ω_{d0} | Ω_e | $\sum m_\nu(\text{eV})$ | n_s | $\frac{dn_s}{d \ln k}$ | $10^{10} \Delta_R^2$ | $\Omega_c h^2$ | $10^3 \Omega_b h^2$ | N_{eff} | τ | Ω_k |
|--|--------|---------------|------------|-------------------------|--------|------------------------|----------------------|----------------|---------------------|------------------|--------|------------|
| PKL $^\kappa$ L $^g + \Omega_k$ | 0.0096 | 0.0021 | 0.0026 | 0.040 | 0.0053 | 0.0022 | 0.20 | 0.0013 | 0.13 | 0.092 | 0.0044 | 0.00056 |
| PKJ $^\kappa$ J $^g + \Omega_k$ | 0.012 | 0.0033 | 0.0032 | 0.047 | 0.0056 | 0.0024 | 0.19 | 0.0013 | 0.14 | 0.092 | 0.0045 | 0.00088 |
| PKL $^\kappa$ L $^g + \Omega_k - \Omega_e$ | 0.0029 | 0.0015 | — | 0.028 | 0.0039 | 0.0019 | 0.18 | 0.0012 | 0.13 | 0.079 | 0.0041 | 0.00056 |
| PKJ $^\kappa$ J $^g + \Omega_k - \Omega_e$ | 0.0045 | 0.0025 | — | 0.026 | 0.0050 | 0.0023 | 0.18 | 0.0013 | 0.14 | 0.085 | 0.0044 | 0.00087 |
| PKL $_{\ell < 1000}^\kappa$ L $_{\ell < 1000}^g + \Omega_k$ | 0.010 | 0.0024 | 0.0027 | 0.042 | 0.0057 | 0.0032 | 0.21 | 0.0013 | 0.14 | 0.10 | 0.0045 | 0.00068 |
| PKJ $_{\ell < 1000}^\kappa$ J $_{\ell < 1000}^g + \Omega_k$ | 0.012 | 0.0037 | 0.0033 | 0.049 | 0.0060 | 0.0036 | 0.20 | 0.0014 | 0.15 | 0.11 | 0.0045 | 0.00098 |
| PKL $_{\ell < 1000}^\kappa$ L $_{\ell < 1000}^g + \Omega_k - \Omega_e$ | 0.0030 | 0.0020 | — | 0.029 | 0.0041 | 0.0031 | 0.18 | 0.0013 | 0.14 | 0.084 | 0.0042 | 0.00066 |
| PKJ $_{\ell < 1000}^\kappa$ J $_{\ell < 1000}^g + \Omega_k - \Omega_e$ | 0.0049 | 0.0029 | — | 0.027 | 0.0053 | 0.0035 | 0.19 | 0.0014 | 0.15 | 0.10 | 0.0044 | 0.00097 |

TABLE VII. Same as Table VI, without SNe.

of 0.03-0.04 eV is possible (see Tables IV and VI). At this level, a detection is possible if the neutrino mass hierarchy is inverted as Fig. 11 shows.

When the early dark energy density and curvature are both fixed, the constraint on sum of neutrino masses is 0.15 eV from Planck alone. This clearly shows that the sum of neutrino masses is substantially correlated with early dark energy. This is also apparent in the right column top panel of Fig. 9 where we plot the constraints in the plane of the sum of neutrino masses and EDE density. Thus, as expected, ignorance of the expansion history at high redshifts can significantly hamper the constraints on the sum of neutrino masses from CMB lensing and cosmic shear. However, the constraints (even in the presence of EDE) can be substantially improved by adding cosmic shear tomography data because the degeneracy direction in cosmic shear data is substantially different from that in CMB lensing (see Fig. 9).

We note here that our estimate of 0.15 eV when

curvature and EDE density are held fixed is based on the assumption that reionization happened sharply, and therefore all of the effects on the CMB can be encapsulated in the optical depth parameter. We also allow for more complicated reionization histories by imposing a floor of $\ell = 30$ in the polarization data and a prior on τ of 0.01 [19]. With this setup, we find that neutrino mass constraints degrade by about 10% (see $P_{\ell > 30\text{K}} + \sigma(\tau)$ cases in Tables IV, VI, V).

We also considered a case assuming sharp reionization where w_0 is held fixed as is EDE density and curvature. In this rather optimistic setup, we obtain an uncertainty of about 0.14 eV for the sum of neutrino masses with Planck lensing. We note that this is about 20% less stringent than the number quoted in Ref. [29], some of which can be traced to their different fiducial cosmology and larger sky fraction (75% vs 65%).

We checked that the cross-correlation of κ_c and T (i.e. without $\kappa_c \kappa_c$) doesn't particularly improve the

| Probe | w_0 | Ω_{d0} | Ω_e | $\sum m_\nu$ (eV) | n_s | $\frac{dn_s}{d \ln k}$ | $10^{10} \Delta_R^2$ | $\Omega_c h^2$ | $10^3 \Omega_b h^2$ | N_{eff} | τ | Ω_k |
|---------------------------------------|-------|---------------|------------|-------------------|--------|------------------------|----------------------|----------------|---------------------|------------------|--------|------------|
| PKL $^\kappa$ + Ω_k | 0.024 | 0.0037 | 0.0040 | 0.068 | 0.0069 | 0.0028 | 0.22 | 0.0018 | 0.19 | 0.12 | 0.0048 | 0.0021 |
| PKJ $^\kappa$ + Ω_k | 0.036 | 0.0053 | 0.0054 | 0.093 | 0.0073 | 0.0035 | 0.23 | 0.0020 | 0.20 | 0.13 | 0.0049 | 0.0022 |
| PKL $^\kappa$ + $\Omega_k - \Omega_e$ | 0.021 | 0.0030 | — | 0.047 | 0.0066 | 0.0028 | 0.22 | 0.0018 | 0.19 | 0.11 | 0.0048 | 0.0021 |
| PKJ $^\kappa$ + $\Omega_k - \Omega_e$ | 0.034 | 0.0046 | — | 0.059 | 0.0071 | 0.0034 | 0.23 | 0.0019 | 0.19 | 0.12 | 0.0049 | 0.0022 |
| PKL g + Ω_k | 0.063 | 0.016 | 0.0056 | 0.078 | 0.0073 | 0.0041 | 0.23 | 0.0020 | 0.20 | 0.14 | 0.0049 | 0.0016 |
| PKJ g + Ω_k | 0.11 | 0.027 | 0.0064 | 0.12 | 0.0076 | 0.0058 | 0.23 | 0.0023 | 0.22 | 0.20 | 0.0049 | 0.0021 |
| PKL g + $\Omega_k - \Omega_e$ | 0.059 | 0.016 | — | 0.074 | 0.0072 | 0.0040 | 0.23 | 0.0020 | 0.20 | 0.14 | 0.0049 | 0.0015 |
| PKJ g + $\Omega_k - \Omega_e$ | 0.098 | 0.025 | — | 0.10 | 0.0073 | 0.0052 | 0.23 | 0.0023 | 0.21 | 0.17 | 0.0049 | 0.0021 |

TABLE VIII. Same as Table VI, but only for combinations of CMB with weak lensing power spectrum measurements, and CMB with galaxy power spectrum measurements.

| Probe | w_0 | Ω_{d0} | Ω_e | $\sum m_\nu$ (eV) | n_s | $\frac{dn_s}{d \ln k}$ | $10^{10} \Delta_R^2$ | $\Omega_c h^2$ | $10^3 \Omega_b h^2$ | N_{eff} | τ | Ω_k |
|---|--------|---------------|------------|-------------------|--------|------------------------|----------------------|----------------|---------------------|------------------|--------|------------|
| PKL $^\kappa$ L g + Ω_k | 0.015 | 0.0030 | 0.0033 | 0.054 | 0.0062 | 0.0024 | 0.23 | 0.0016 | 0.21 | 0.11 | 0.0051 | 0.0015 |
| PKJ $^\kappa$ J g + Ω_k | 0.022 | 0.0045 | 0.0047 | 0.071 | 0.0073 | 0.0031 | 0.24 | 0.0020 | 0.24 | 0.13 | 0.0053 | 0.0021 |
| PKL $^\kappa$ L g L s + Ω_k | 0.012 | 0.0025 | 0.0029 | 0.051 | 0.0059 | 0.0024 | 0.23 | 0.0016 | 0.20 | 0.11 | 0.0051 | 0.0014 |
| PKJ $^\kappa$ J g J s + Ω_k | 0.010 | 0.0027 | 0.0038 | 0.066 | 0.0069 | 0.0031 | 0.24 | 0.0019 | 0.23 | 0.12 | 0.0053 | 0.0020 |
| PKL $^\kappa$ $_{\ell < 1000}$ L g $_{\ell < 1000}$ + Ω_k | 0.017 | 0.0037 | 0.0037 | 0.059 | 0.0066 | 0.0032 | 0.23 | 0.0017 | 0.20 | 0.13 | 0.0052 | 0.0015 |
| PKJ $^\kappa$ $_{\ell < 1000}$ J g $_{\ell < 1000}$ + Ω_k | 0.027 | 0.0063 | 0.0053 | 0.082 | 0.0076 | 0.0048 | 0.24 | 0.0022 | 0.24 | 0.18 | 0.0053 | 0.0020 |
| PKL $^\kappa$ $_{\ell < 1000}$ L g $_{\ell < 1000}$ L s + Ω_k | 0.012 | 0.0029 | 0.0033 | 0.056 | 0.0064 | 0.0032 | 0.23 | 0.0017 | 0.20 | 0.13 | 0.0052 | 0.0014 |
| PKJ $^\kappa$ $_{\ell < 1000}$ J g $_{\ell < 1000}$ J s + Ω_k | 0.011 | 0.0030 | 0.0047 | 0.079 | 0.0074 | 0.0047 | 0.24 | 0.0022 | 0.23 | 0.18 | 0.0053 | 0.0020 |
| PKL $^\kappa$ L g + $\Omega_k - \Omega_e$ | 0.0094 | 0.0023 | — | 0.036 | 0.0048 | 0.0023 | 0.22 | 0.0016 | 0.19 | 0.091 | 0.0050 | 0.0014 |
| PKJ $^\kappa$ J g + $\Omega_k - \Omega_e$ | 0.015 | 0.0037 | — | 0.043 | 0.0066 | 0.0031 | 0.24 | 0.0020 | 0.23 | 0.11 | 0.0053 | 0.0021 |
| PKL $^\kappa$ L g L s + $\Omega_k - \Omega_e$ | 0.0081 | 0.0022 | — | 0.036 | 0.0048 | 0.0023 | 0.22 | 0.0016 | 0.19 | 0.091 | 0.0050 | 0.0014 |
| PKJ $^\kappa$ J g J s + $\Omega_k - \Omega_e$ | 0.0081 | 0.0026 | — | 0.042 | 0.0065 | 0.0031 | 0.24 | 0.0019 | 0.22 | 0.11 | 0.0053 | 0.0020 |
| PKL $^\kappa$ $_{\ell < 1000}$ L g $_{\ell < 1000}$ + $\Omega_k - \Omega_e$ | 0.012 | 0.0034 | — | 0.036 | 0.0052 | 0.0032 | 0.22 | 0.0017 | 0.18 | 0.10 | 0.0051 | 0.0014 |
| PKJ $^\kappa$ $_{\ell < 1000}$ J g $_{\ell < 1000}$ + $\Omega_k - \Omega_e$ | 0.021 | 0.0059 | — | 0.044 | 0.0067 | 0.0045 | 0.24 | 0.0022 | 0.22 | 0.14 | 0.0053 | 0.0020 |
| PKL $^\kappa$ $_{\ell < 1000}$ L g $_{\ell < 1000}$ L s + $\Omega_k - \Omega_e$ | 0.0092 | 0.0028 | — | 0.036 | 0.0052 | 0.0032 | 0.22 | 0.0017 | 0.18 | 0.10 | 0.0051 | 0.0014 |
| PKJ $^\kappa$ $_{\ell < 1000}$ J g $_{\ell < 1000}$ J s + $\Omega_k - \Omega_e$ | 0.0084 | 0.0030 | — | 0.043 | 0.0067 | 0.0044 | 0.24 | 0.0021 | 0.22 | 0.14 | 0.0053 | 0.0020 |

TABLE IX. Same as Tables VI and VII, without any cross-correlations between the observables (except for tomographic ones within a survey).

constraint on the sum of neutrino masses, but it improves the constraint on the late time dark energy density and EOS by about 50% compared to temperature and polarization data alone.

Compared to the CMB with lensing, the LSST constraint on the sum of neutrino masses is moderately weaker for both galaxy tomography (by 50%) and weak lensing tomography (by 25%), whereas the JDEM constraint on the sum of neutrino masses is a factor of three weaker for galaxy tomography and a factor of two weaker for weak lensing tomography. In analyzing all the probes allowing for EDE density to vary, we find a one-sigma constraint of 0.03-0.04 eV for LSST and JDEM (see Table IV). Tables VII and IX show that the strength of JDEM in this joint analysis is owed partly to the superior SN constraints on the dark energy EOS (which helps in breaking degeneracies) and partly to the cross-correlations between the temperature, lensing, and galaxy fields.

Given the recent 2σ indications of extra relativistic species in the universe (e.g. $N_{\text{eff}} = 3.86 \pm 0.42$ with

the datasets WMAP7+SPT+HST+BAO for a minimal cosmology [158]; for extended parameter spaces see [159]), our understanding of N_{eff} depends critically on the ability to distinguish its signatures from other cosmological parameters. Fortunately, even for our extended parameter spaces, Planck alone could determine the possible existence of extra relativistic species in the universe at the 4σ level, as seen in Tables V and VI. The constraints on N_{eff} are only weakly correlated with the constraints on $\sum m_\nu$, as shown in Fig. 12. When Planck is combined with JDEM or LSST, this allows for a more than 10σ detection of additional light degrees of freedom in our universe.

Turning our attention to systematics, Table IV shows that the different choices for nonlinear cutoffs in $\ell_{\text{max}} \in [1000, 3000]$ do not significantly affect the combined constraints. We can therefore throw out highly nonlinear scales ($\ell > 1000$) without significant loss in the parameter constraints shown in this work. This is primarily due to the combination of cosmological probes and to a lesser extent, due to the

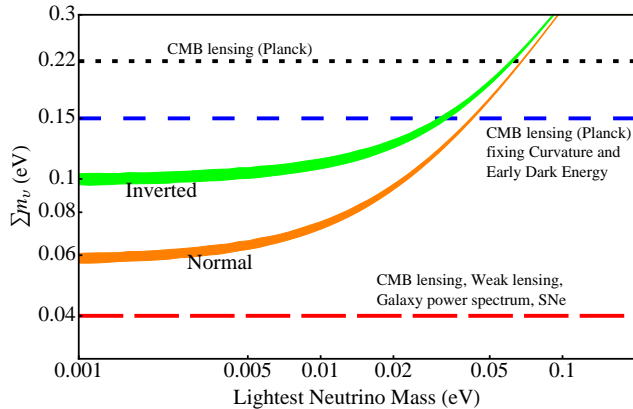


FIG. 11. Bands show the allowed values for the sum of neutrino masses as a function of the lightest neutrino mass eigenstate. The branch with higher values is for the inverted mass hierarchy. We have used the constraints on the neutrino mass squared differences from the Particle Data Group [153] to create bands of the allowed regions. The 3 horizontal lines show the 1σ Fisher matrix error estimates for the cases PK + Ω_k (0.22 eV, Table VI), PK - Ω_e (0.15 eV, Table V) and PKL^sL^lL^s + Ω_k (0.04 eV, Table VI).

cross-correlations we have introduced. For comparison, considering only one probe, the constraint degradation could be up to a factor of 3 in dark energy and neutrino mass parameters (Table IV). This insensitivity to nonlinear scales is maintained even without SN measurements (Table VII).

Comparing Table IV with Table VI, i.e. comparing constraints for a flat universe with a universe that allows for a possible non-zero curvature, shows the CMB temperature, polarization, and lensing constraints on Ω_k from Planck improve by an order of magnitude when accounting for future weak lensing, galaxy clustering, and supernova measurements from LSST or JDEM. The SN measurements are, as expected, most sensitive to the curvature prior, exhibiting significant degradations in parameters across the board. This motivates the consistent use of a CMB curvature prior for SN measurements. The parameter that the SN observations with a JDEM-like survey measure well is the dark energy EOS (the relative weakness of SNe from LSST is explained in Sec. III). Tables VI and VII show that the neglect of SN observations has $< 10\%$ impact on the cosmological constraints for LSST, whereas for a JDEM survey the dark energy parameters degrade by up to 50% without SN measurements. The same features are found in the scenarios with an $\ell_{\max} = 1000$ nonlinear cutoff in multipole space.

Tables VI and IX show that most parameters improve by 20% - 40% when cross-correlations are included for LSST. The cross-correlations have a greater impact for JDEM than for LSST. In particular, the early dark energy density, baryon and CDM densities, and sum of neutrino mass constraints improve by up to factor of 2 with cross-correlations, the curvature

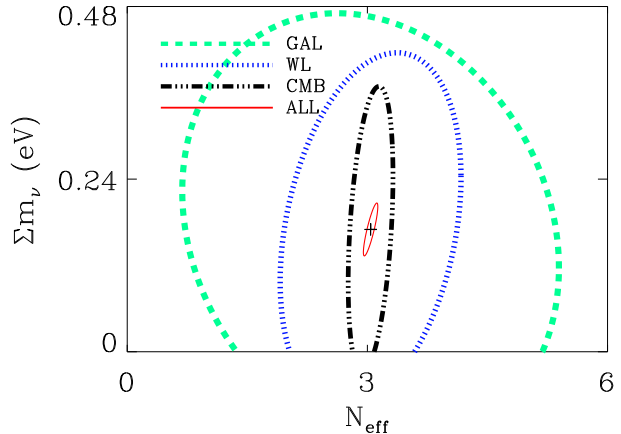


FIG. 12. Error ellipses showing degeneracies between the sum of neutrino masses (Σm_ν) and the effective number of neutrinos (N_{eff}) in a flat universe, where we have marginalized over the early dark energy density. The curves have the same meaning as in Fig. 9. Even for our extended parameter spaces, the CMB temperature as measured by Planck will be able to determine the possible existence of extra relativistic species, while the combination of experimental probes is extremely helpful in pinning down the sum of neutrino masses.

density constraint improves by factor of 3 (also for LSST), while the improvement in the other parameters are at the same 20% - 40% level as for LSST. Naturally, when we weaken the parameter constraints by imposing $\ell_{\max} = 1000$ in galaxy and lensing tomography, the impact of the cross-correlations increases somewhat (e.g. an additional 20% in early dark energy and sum of neutrino masses for JDEM). These quantitative comparisons between a full covariance and one without cross-correlations largely hold true independently of the SN sample. In the final analysis with all cross-correlations, both JDEM and LSST are expected to provide similar parameter constraints even though the individual constraints and systematics are different.

We now turn attention to the impact of keeping EDE fixed. In Table V we explore the case where EDE exists but is kept fixed for the Fisher matrix analysis. We expect this to mimic the analysis where the existence of EDE is neglected. We explore biases resulting from such a scenario in the ensuing section. We expect the constraints in this limit (of keeping Ω_e fixed) to match the constraints in a non-EDE cosmology, i.e., the standard case with $\Omega_e = 0$. Table V shows that the CMB temperature and polarization constraints on cosmology are nearly unaffected ($\lesssim 10\%$ differences) by the removal of EDE. The removal of EDE improves the sum of neutrino masses by 30%, and most other parameter constraints by $\lesssim 10\%$ when CMB lensing is included.

If we turn to the non-CMB probes, we find that significant degeneracies with Ω_e exist for the dark energy parameters, sum of neutrino masses, and the parameters determining the normalization, spectral index,

| Probe | w_0 | Ω_{d0} | Ω_e | $\sum m_\nu$ (eV) | n_s | $\frac{dn_s}{d \ln k}$ | $10^{10} \Delta_R^2$ | $\Omega_c h^2$ | $10^3 \Omega_b h^2$ | N_{eff} | τ | Ω_k |
|---|--------|---------------|------------|-------------------|--------|------------------------|----------------------|----------------|---------------------|------------------|--------|------------|
| P + Ω_k | 0.21 | 0.042 | 0.0041 | 0.32 | 0.0042 | 0.0049 | 0.15 | 0.0017 | 0.082 | 0.14 | 0.0031 | 0.0069 |
| PK + Ω_k | 0.092 | 0.024 | 0.0038 | 0.079 | 0.0040 | 0.0044 | 0.14 | 0.0013 | 0.077 | 0.11 | 0.0029 | 0.0024 |
| PKL ^{κ} L ^g L ^s + Ω_k | 0.0062 | 0.0015 | 0.0017 | 0.027 | 0.0035 | 0.0015 | 0.13 | 0.00074 | 0.064 | 0.052 | 0.0027 | 0.00046 |
| PKJ ^{κ} J ^g J ^s + Ω_k | 0.0065 | 0.0019 | 0.0020 | 0.029 | 0.0037 | 0.0019 | 0.13 | 0.00088 | 0.066 | 0.058 | 0.0028 | 0.00061 |
| PKL ^{κ} _{$\ell < 1000$} L ^g _{$\ell < 1000$} L ^s + Ω_k | 0.0065 | 0.0016 | 0.0018 | 0.028 | 0.0036 | 0.0024 | 0.13 | 0.00076 | 0.066 | 0.061 | 0.0028 | 0.00051 |
| PKJ ^{κ} _{$\ell < 1000$} J ^g _{$\ell < 1000$} J ^s + Ω_k | 0.0067 | 0.0020 | 0.0021 | 0.030 | 0.0038 | 0.0029 | 0.13 | 0.00097 | 0.067 | 0.069 | 0.0028 | 0.00065 |

TABLE X. Same as Table VI, except for a 2m EPIC survey in lieu of Planck.

| Probe | w_0 | Ω_{d0} | Ω_e | $\sum m_\nu$ | n_s | $\frac{dn_s}{d \ln k}$ | $10^{10} \Delta_R^2$ | $\Omega_c h^2$ | $10^3 \Omega_b h^2$ | N_{eff} | τ |
|--|-------|---------------|------------|--------------|-------|------------------------|----------------------|----------------|---------------------|------------------|--------|
| PKL ^{κ} L ^g - Ω_e | 0.83 | 0.45 | — | 0.23 | 0.41 | 0.091 | 0.37 | 0.40 | 0.061 | 0.41 | 0.29 |
| PKJ ^{κ} J ^g - Ω_e | 2.4 | 1.5 | — | 0.17 | 0.35 | 0.27 | 0.73 | 0.34 | 0.029 | 0.39 | 0.48 |

TABLE XI. We present the fractional bias $|\delta(p_i)|/\sigma(p_i)$ (see Eqn. 49) on cosmological parameters for the full combination of lensing, galaxy, and CMB surveys up to $\ell = 2000$. The letters [L, J] in the first column denote [LSST, JDEM] (precise explanation of notation in caption of Table IV). The parameter biases are comparable for Planck and EPIC. In this table, we assume a flat fiducial universe with $\Omega_e = 0.01$, and determine the offset in the parameter estimates for the case where EDE is not accounted for in the analysis. Naturally, the bias is larger for a universe with a larger fraction of EDE.

and its running of the matter power spectrum, as expected from Fig. 2. For instance, for weak lensing with both LSST and JDEM, the power spectrum normalization constraint improves by more than a factor of two without EDE, the present DE EOS improves by 70%, the running by 50%, the sum of neutrino masses and spectral index by 30%, and the present DE density by 20%. When we throw out nonlinear scales ($\ell_{\text{max}} = 1000$), the constraint on the sum of neutrino masses only improves by about 5%. This is because the sum of neutrino masses derives its degeneracy with the EDE density from small angular scales, as also illustrated by the respective parameter derivatives in Fig. 4.

In SN measurements, we find the strongest degeneracy between the present dark energy density and the early dark energy density, which degrades the constraint on the present DE density by factor of five in LSST and factor of seven in JDEM. In the joint observational analysis of prospective cosmological constraints, we also find that our ignorance of EDE significantly degrades our constraints on the other cosmological parameters. As an example, when keeping Ω_e fixed in Table V, the DE EOS constraint of $\sigma(w_0) \simeq 3 \times 10^{-3}$ (for both LSST and JDEM) has improved by a factor of 3 for LSST and factor of 2 for JDEM. In Table VII, we find these degradations would have been stronger if SN observations were not considered in the analysis. We further note that this 0.3% constraint on the EOS may be translated into roughly 10 model-independent redshift bins each constrained at the 1% level (since $\sum_i \sigma^{-2}(w_i) = \sigma^{-2}(w)$ [49], where w_i are binned EOS parameters and w refers to a constant EOS). Thus, if the dark energy EOS varies at late times, there is significant promise in detecting its variation with our considered surveys.

To end this section, we consider the constraints achievable with a future CMB mission such as the 2m EPIC (EPIC-2m) proposal [100, 101] in Table X. The properties of this probe are listed in Table III. With up to 40% increased resolution and factor of thirty lower noise in an individual band than Planck, the EPIC-2m survey in Table X shows improved constraints across the board compared to Planck. The joint observational constraints, with EPIC-2m in lieu of Planck, also show significant gains – about 30% improvement in the DE constraints, about 40% improvement in the sum of neutrino masses constraint, and up to a factor of two improvement in the other parameters.

C. Dark Energy Bias

We have analyzed the expected constraints on early dark energy from use of weak lensing tomography, galaxy tomography, SNe, and CMB. If we live in a universe with EDE but do not account for this in the analysis of the data sets of these future probes, we will compute cosmological parameter constraints that are not only overly optimistic, but the best estimates of the parameters will also be shifted.

We estimate here the parameter bias that would arise from assuming a fiducial universe with $\Omega_e = 0.01$, but where EDE is not accounted for in the constraint analysis. The bias in each parameter is given by [133, 160–162]:

$$\delta p_\alpha = F_{\alpha\beta}^{-1} \sum_{l,\beta} \Delta\ell \times \text{Tr} \left[\tilde{\mathbf{C}}_\ell^{-1} \frac{\partial \mathbf{C}_\ell}{\partial p_\beta} \tilde{\mathbf{C}}_\ell^{-1} \delta C_\ell \right], \quad (49)$$

where δC_ℓ accounts for the difference between the convergence spectra in a universe with EDE and a universe without EDE.

Table XI presents the cosmological parameter biases for the LSST and JDEM surveys combined with Planck (comparable biases when combined with EPIC). For LSST, we find less than 50% bias in most parameters except for w_0 (about 80%). Biases when including JDEM instead of LSST are close to a factor of 2 times the expected constraints for the present DE density and EOS. We note here that these estimates for the biases assume a fiducial cosmology with $\Omega_e = 0.01$. The biases would be larger in a universe with a larger fraction of EDE. If we are to avoid significant bias in future joint analyses of cosmological parameters, we must account for the uncertain high redshift nature of the dark energy component.

IV. CONCLUSIONS

It is conceivable that in order to resolve the nature of the force behind the late-time acceleration of the universe, we need a deeper understanding of how the universal expansion and growth of structure was affected by the dark energy at earlier times. We have chosen an approach that combines probes with varying degrees of sensitivity in different parts of cosmological parameter space, and we have included the cross-correlations between different probes. We have performed a joint Fisher matrix analysis of prospective measurements of weak lensing tomography, galaxy tomography, SNe, and Planck CMB.

Our results show that the best possible constraints on $[w_0, \Omega_{d0}, \Omega_e, \sum m_\nu(\text{eV}), n_s, \frac{dn_s}{d \ln k}, 10^{10} \Delta_R^2, \Omega_c h^2, 10^3 \Omega_b h^2, N_{\text{eff}}, \tau, \Omega_k]$ will be at the level of $[0.0085, 0.0019, 0.0023, 0.038, 0.0051, 0.0021, 0.20, 0.0013, 0.13, 0.090, 0.0044, 0.00056]$ for a wide survey like LSST, and $[0.0076, 0.0021, 0.0025, 0.036, 0.0055, 0.0024, 0.19, 0.0012, 0.14, 0.090, 0.0045, 0.00075]$ for a deep survey like JDEM. These constraints assume that photometric redshift and other systematic uncertainties in weak lensing can be controlled to better than 0.1%. Naturally, these constraints improve in a universe without EDE. For constraints on our extended parameter space with present cosmological datasets, see Ref. [159].

Our main findings are summarized below.

- The dominant constraint on the fraction of dark energy at early times comes from the CMB (in particular TT and to some extent $T\kappa_c$). Constraints from Planck are expected to be within a percent of the critical density. The next best probe of EDE is weak lensing tomography, followed by galaxy tomography, and then SNe. When all 6 observables (CMB temperature T , CMB polarization E , CMB lensing κ_c , weak lensing shear κ , galaxy counts g , SNe s) and all relevant cross-correlations (see Eqns. 47-48) are analyzed in a combined setting, the constraint on Ω_e improves by a factor of four over

the CMB constraint. Interestingly, due to the cross-correlations, the combined constraints are equally strong for LSST and JDEM (κ, g, s).

- When analyzed together with early dark energy, we find that the sum of active neutrino masses is most strongly constrained by the CMB lensing potential power spectrum, at the level of 0.22 eV for Planck (0.20 eV when flatness assumed) and 0.08 eV for Epic (0.07 eV when flatness assumed). A combined analysis of Planck, and LSST or JDEM, shows that future constraints at the level of 0.04 eV are possible. The CMB lensing constraints improve by 30%, and the combined constraints by 60%, when EDE is not allowed to vary. Our results suggest that these constraints are not significantly affected by our ignorance of the reionization history, but more detailed work on this issue is necessary.
- The additional degree of freedom from the early dark energy density degrades our ability to measure late-time dark energy. We find that the present DE density can be measured to 0.2% of the critical density and equation of state to about 0.01, which is a factor of roughly 2 and 3 degradation, respectively, in the constraints compared to the case when EDE is fixed.
- Our analysis suggests that throwing out nonlinear scales ($\ell > 1000$) may not result in significant degradation in future parameter measurements when multiple cosmological probes are combined. Including cross-correlations improves parameter constraints on dark energy density and sum of neutrino masses by up to a factor of 2 when these nonlinear scales are not included.
- The curvature of the universe can be constrained to 6×10^{-3} of the critical density from CMB temperature and lensing alone, and improved by an order of magnitude in the joint analysis in agreement with the results of Ref. [157]. Measurement of the curvature of the universe with Planck will be good enough that weak lensing tomography, galaxy tomography, and supernova measurements will not be limited by our ignorance of the curvature.
- Even a modest 1% of the critical density at high redshift in dark energy, if not accounted for, shifts cosmological parameters by 1-2 σ . Therefore, it is crucial for measurements of the underlying cosmology that we avoid prejudices about the energy content of the high redshift universe.

We have shown that degeneracies between cosmological parameters, in particular between early dark energy, curvature and sum of neutrino masses, can be effectively broken by a joint analysis of weak lensing tomography, galaxy tomography, SNe, and the CMB

(temperature, polarization, lensing). Our analysis included the cross-correlations between these different probes. We find that simultaneous measurements of dark energy density at present and at high redshift with a precision of 0.2% of the respective critical densities, present dark energy equation of state with a precision of 0.01, curvature with a precision of 0.06% of the present critical density, and sum of neutrino masses with a precision of 0.04 eV are possible.

Acknowledgements: We thank Ujjaini Alam and James Bullock for discussions at an early stage of this work. We also thank Alexandre Amblard, Francesco De Bernardis, Gregory D. Martinez, Quinn Minor, Paolo Serra, and Joseph Smidt for useful discussions. SJ acknowledges support from the US Dept. of Education through GAANN at UCI. MK acknowledges support from NSF through grant 0855462 at UCI.

-
- [1] Riess, A. G., *et al.*, *Astron. J.*, **116**, 1009 (1998).
 [2] Perlmutter, S., *et al.*, *Astrophys. J.*, **517**, 565 (1999).
 [3] Dunkley, J., *et al.*, *Astrophys. J. Suppl.*, **180**, 306 (2009).
 [4] Komatsu, E., *et al.*, *Astrophys. J. Suppl.*, **180**, 330 (2009).
 [5] M. Tegmark *et al.* [SDSS Collaboration], *Astrophys. J.* **606**, 702 (2004).
 [6] M. Tegmark *et al.* [SDSS Collaboration], *Phys. Rev. D* **74**, 123507 (2006).
 [7] S. Cole *et al.* [The 2dFGRS Collaboration], *Mon. Not. Roy. Astron. Soc.* **362**, 505 (2005).
 [8] R. R. Caldwell, R. Dave, P. J. Steinhardt, *Phys. Rev. Lett.* **80**, 1582-1585 (1998).
 [9] Wetterich, C., *Nucl. Phys. B*, **302**, 668 (1988).
 [10] I. Zlatev, L. M. Wang and P. J. Steinhardt, *Phys. Rev. Lett.* **82**, 896 (1999) [arXiv:astro-ph/9807002].
 [11] P. G. Ferreira and M. Joyce, *Phys. Rev. D* **58**, 023503 (1998) [arXiv:astro-ph/9711102].
 [12] T. Chiba, N. Sugiyama and T. Nakamura, *Mon. Not. Roy. Astron. Soc.* **289**, L5 (1997) [arXiv:astro-ph/9704199].
 [13] P. J. E. Peebles and B. Ratra, *Astrophys. J.* **325**, L17 (1988).
 [14] B. Ratra and P. J. E. Peebles, *Phys. Rev. D* **37**, 3406 (1988).
 [15] L. H. Ford, *Phys. Rev. D* **35**, 2339 (1987).
 [16] S. Dodelson, M. Kaplinghat, E. Stewart, *Phys. Rev. Lett.* **85**, 5276-5279 (2000).
 [17] Linder, E. V., Robbers, G., *JCAP*, **06**, 004 (2008).
 [18] Doran, M., Robbers, G., *JCAP*, **06**, 026 (2006).
 [19] M. Kaplinghat, L. Knox, Y. -S. Song, *Phys. Rev. Lett.* **91**, 241301 (2003).
 [20] J. Lesgourgues, L. Perotto, S. Pastor and M. Piat, *Phys. Rev. D* **73**, 045021 (2006).
 [21] A. R. Cooray, *Astron. Astrophys.* **348**, 31 (1999).
 [22] K. N. Abazajian, S. Dodelson, *Phys. Rev. Lett.* **91**, 041301 (2003).
 [23] Hannestad, S., Tu, H., Wong, Y., *JCAP*, **06**, 025 (2006).
 [24] J. Lesgourgues, S. Pastor and L. Perotto, *Phys. Rev. D* **70**, 045016 (2004).
 [25] S. Hannestad, *Phys. Rev. D* **67**, 085017 (2003).
 [26] W. Hu, D. J. Eisenstein and M. Tegmark, *Phys. Rev. Lett.* **80**, 5255 (1998).
 [27] D. J. Eisenstein, W. Hu and M. Tegmark, *Astrophys. J.* **518**, 2 (1999).
 [28] T. Namikawa, S. Saito and A. Taruya, *JCAP* **1012**, 027 (2010).
 [29] R. de Putter, O. Zahn and E. V. Linder, *Phys. Rev. D* **79**, 065033 (2009).
 [30] Doran, M., Robbers, G., Wetterich, C., *Phys. Rev. D*, **75**, 023003 (2007).
 [31] Caldwell, R., *et al.*, *Astrophys. J.*, **591**, L75 (2003).
 [32] M. J. Francis, G. F. Lewis and E. V. Linder, *Mon. Not. Roy. Astron. Soc. Lett.* **393**, L31 (2008).
 [33] M. J. Francis, G. F. Lewis and E. V. Linder, *Mon. Not. Roy. Astron. Soc.* **394**, 605 (2008).
 [34] M. Grossi and V. Springel, *Mon. Not. Roy. Astron. Soc.* **394**, 1559 (2009).
 [35] J. -Q. Xia and M. Viel, *JCAP* **0904**, 002 (2009).
 [36] L. Hollenstein, D. Sapone, R. Crittenden and B. M. Schaefer, *JCAP* **0904**, 012 (2009).
 [37] J. Lesgourgues, S. Pastor, *Phys. Rept.* **429**, 307-379 (2006).
 [38] M. Kaplinghat, M. Chu, Z. Haiman, G. Holder, L. Knox, C. Skordis, *Astrophys. J.* **583**, 24-32 (2003).
 [39] G. Holder, Z. Haiman, M. Kaplinghat, L. Knox, *Astrophys. J.* **595**, 13-18 (2003).
 [40] W. Hu, G. P. Holder, *Phys. Rev. D* **68**, 023001 (2003). [astro-ph/0303400].
 [41] A. Albrecht, C. Skordis, *Phys. Rev. Lett.* **84**, 2076-2079 (2000).
 [42] K. Griest, *Phys. Rev. D* **66**, 123501 (2002).
 [43] C. Skordis, A. Albrecht, *Phys. Rev. D* **66**, 043523 (2002).
 [44] C. P. Ma, R. R. Caldwell, P. Bode and L. M. Wang, *Astrophys. J.* **521**, L1 (1999).
 [45] <http://camb.info>
 [46] Fang, W., Hu, W., Lewis, A., *Phys. Rev. D.*, **78**, 087303 (2008).
 [47] Smith, R. E., *et al.*, *MNRAS*, **341**, 1311 (2003).
 [48] McDonald, P., Trac, H., Contaldi, C., *MNRAS*, **366**, 547 (2006).
 [49] S. Joudaki, A. Cooray and D. E. Holz, *Phys. Rev. D* **80**, 023003 (2009).
 [50] S. Saito, M. Takada and A. Taruya, *Phys. Rev. Lett.* **100**, 191301 (2008).
 [51] J. Brandbyge, S. Hannestad, T. Haugboelle and B. Thomsen, *JCAP* **0808**, 020 (2008).
 [52] Y. Y. Y. Wong, *JCAP* **0810**, 035 (2008).
 [53] S. Saito, M. Takada and A. Taruya, *Phys. Rev. D* **80**, 083528 (2009).
 [54] S. Dodelson, *Modern Cosmology* (Academic Press, San Diego, 2003).
 [55] Refregier, A., *Ann. Rev. Astron. Astrophys.*, **41**, 645 (2003).
 [56] Bartelmann, M., Schneider, P., *Phys. Rept.*, **340**, 291 (2001).
 [57] Wittman, D. M., *et al.*, *Nature*, **405**, 143 (2000).
 [58] Jarvis, M., *et al.*, *Astrophys. J.*, **644**, 71 (2006).
 [59] Hoekstra, H., *et al.*, *Astrophys. J.*, **647**, 116 (2006).

- [60] Kaiser, N., Wilson, G., Luppino, G. A., arXiv:astro-ph/0003338v1 (2000).
- [61] Bacon, D., Refregier, A., Ellis, R., MNRAS, **318**, 625 (2000).
- [62] van Waerbeke, L., *et al.*, A&A, **358**, 30 (2000).
- [63] Heymans, C., *et al.*, MNRAS, **361**, 160 (2005).
- [64] Brown, M. L., *et al.*, MNRAS, **341**, 100 (2003).
- [65] van Waerbeke, L., Mellier, Y., Hoekstra, H., A&A, **429**, 75 (2005).
- [66] Albrecht, A., *et al.*, arXiv:astro-ph/0609591.
- [67] Ma, Z., Hu, W., Huterer, D., Astrophys. J., **636**, 21 (2005).
- [68] Hu, W., Astrophys. J. **522**, L21 (1999).
- [69] Cooray, A., Hu, W., Astrophys. J., **574**, 19 (2002).
- [70] Shapiro, C., Cooray, A., JCAP, **03**, 007 (2006).
- [71] Hirata, C., Seljak, U., Phys. Rev. D, **68**, 083002 (2003).
- [72] W. Hu, Phys. Rev. D **62**, 043007 (2000).
- [73] N. Kaiser, Astrophys. J. **388**, 272 (1992).
- [74] D. Limber, Astrophys. J. **119**, 655 (1954).
- [75] Hu, W., Jain, B., Phys. Rev. D, **70**, 043009 (2004).
- [76] H. Zhan, JCAP **0608**, 008 (2006).
- [77] M. Schneider, L. Knox, H. Zhan and A. Connolly, Astrophys. J. **651**, 14 (2006).
- [78] D. H. Weinberg, R. Dave, N. Katz and L. Hernquist, Astrophys. J. **601**, 1 (2004).
- [79] Lewis, A., Challinor, A., Lasenby, A., Astrophys. J., **538**, 473 (2000).
- [80] M. Zaldarriaga and U. Seljak, Phys. Rev. D **58**, 023003 (1998).
- [81] U. Seljak, Astrophys. J. **463**, 1 (1996).
- [82] J. Smidt, A. Cooray, A. Amblard, S. Joudaki, D. Munshi, M. G. Santos and P. Serra, Astrophys. J. **728**, L1 (2011).
- [83] S. Das *et al.*, arXiv:1103.2124 [astro-ph.CO].
- [84] R. K. Sachs and A. M. Wolfe, Astrophys. J. **147**, 73 (1967) [Gen. Rel. Grav. **39**, 1929 (2007)].
- [85] P. Fosalba, E. Gaztanaga and F. Castander, Astrophys. J. **597**, L89 (2003).
- [86] T. Giannantonio, R. Scranton, R. G. Crittenden, R. C. Nichol, S. P. Boughn, A. D. Myers and G. T. Richards, Phys. Rev. D **77**, 123520 (2008).
- [87] S. Ho, C. Hirata, N. Padmanabhan, U. Seljak and N. Bahcall, Phys. Rev. D **78**, 043519 (2008).
- [88] A. J. Nishizawa, E. Komatsu, N. Yoshida, R. Takahashi and N. Sugiyama, arXiv:0711.1696 [astro-ph].
- [89] Sarkar, D., *et al.*, Phys. Rev. Lett., **100**, 241302 (2008).
- [90] Aldering, G., *et al.*, Proc. SPIE, **4836**, 61 (2002).
- [91] G. Aldering, *et al.*, astro-ph/0405232 (2004).
- [92] [LSST Science Collaborations and LSST Project Collaboration], arXiv:0912.0201 [astro-ph.IM].
- [93] Kim, A. G., *et al.*, MNRAS, **347**, 909 (2004).
- [94] Linder, E. V., Huterer, D., Phys. Rev. D, **67**, 081303 (2003).
- [95] D. Huterer and M. S. Turner, Phys. Rev. D **64**, 123527 (2001).
- [96] A. G. Kim, E. V. Linder, R. Miquel and N. Mostek, Mon. Not. Roy. Astron. Soc. **347**, 909 (2004).
- [97] J. A. Frieman, D. Huterer, E. V. Linder and M. S. Turner, Phys. Rev. D **67**, 083505 (2003).
- [98] <http://www.esa.int/planck>
- [99] G. Efstathiou, *et al.*, *Planck: The Scientific Programme* (Blue Book), ESA-SCI 1 (2005).
- [100] J. Bock *et al.* [EPIC Collaboration], arXiv:0906.1188 [astro-ph.CO].
- [101] D. Baumann *et al.* [CMBPol Study Team Collaboration], AIP Conf. Proc. **1141**, 10 (2009) [arXiv:0811.3919 [astro-ph]].
- [102] <http://www.lsst.org>
- [103] Zhan, H., Knox, L., Tyson, J. A., Astrophys. J. **690**, 923 (2009).
- [104] Refregier, A., *et al.*, Astron. J., **127**, 3102 (2004).
- [105] <http://universe.nasa.gov/program/probes/jdem.html>; <http://snap.lbl.gov>.
- [106] <http://jdem.gsfc.nasa.gov>
- [107] <http://wfirst.gsfc.nasa.gov>
- [108] Gehrels, N., *et al.*, Final Report of the Joint Dark Energy Mission Science Coordination Group, http://wfirst.gsfc.nasa.gov/science/SCG_Report.pdf
- [109] <http://sci.esa.int/euclid>
- [110] A. Cimatti, *et al.*, arXiv:0912.0914 [astro-ph.CO].
- [111] Ivezić, Z., *et al.*, arXiv:0805.2366v1 (2008).
- [112] Scoccimarro, R., Zaldarriaga, M., Hui, L., Astrophys. J., **527**, 1 (1999).
- [113] Cooray, A., Hu, W., Astrophys. J., **554**, 56 (2001).
- [114] Takada, M., Jain, B., arXiv:0810.4170v1 (2008).
- [115] Zhan, H., Knox, L., Astropart. Phys., **616**, L75 (2004).
- [116] White, M., Astropart. Phys., **22**, 211 (2004).
- [117] M. P. van Daalen, J. Schaye, C. M. Booth and C. D. Vecchia, arXiv:1104.1174 [astro-ph.CO].
- [118] E. Semboloni, H. Hoekstra, J. Schaye, M. P. van Daalen and I. J. McCarthy, arXiv:1105.1075 [astro-ph.CO].
- [119] M. LoVerde and N. Afshordi, Phys. Rev. D **78**, 123506 (2008).
- [120] R. E. Smith, C. Hernandez-Monteagudo and U. Seljak, Phys. Rev. D **80**, 063528 (2009).
- [121] A. Rassat *et al.*, arXiv:0810.0003 [astro-ph].
- [122] Huterer, D., *et al.*, MNRAS, **366**, 101 (2006).
- [123] Hirata, C. M., Seljak, U., Phys. Rev. D, **70**, 063526 (2004).
- [124] S. Bridle, *et al.*, NJP, **9**, 444 (2007).
- [125] B. Joachimi, *et al.*, A&A **523**, A1 (2010).
- [126] T. D. Kitching, A. N. Taylor and A. F. Heavens, Mon. Not. Roy. Astron. Soc. **389** (19??) [arXiv:0801.3270 [astro-ph]].
- [127] C. Heymans *et al.*, MNRAS **371**, 750 (2006).
- [128] M. D. Schneider, *et al.*, arXiv:0903.3870.
- [129] Huterer, D., Takada, M., Astropart. Phys., **23**, 369 (2005).
- [130] Rudd, D., Zentner, A. R., Kravtsov, A.V., Astrophys. J., **672**, 19 (2008).
- [131] Huterer, D., Phys. Rev. D, **65**, 063001 (2002).
- [132] A. R. Zentner, D. H. Rudd and W. Hu, Phys. Rev. D **77**, 043507 (2008).
- [133] C. Shapiro, Astrophys. J. **696**, 775 (2009).
- [134] Dodelson, S., Shapiro, C., White, M., Phys. Rev. D, **73**, 023009 (2006).
- [135] L. J. King and P. Schneider, Astron. Astrophys. **398**, 23 (2003).
- [136] L. King and P. Schneider, Astron. Astrophys. **396**, 411 (2002).
- [137] C. Heymans and A. Heavens, astro-ph/0310495.
- [138] L. J. King, [astro-ph/0506441].
- [139] B. Joachimi and P. Schneider, arXiv:0804.2292 [astro-ph].
- [140] P. Zhang, Astrophys. J. **720**, 1090 (2010).
- [141] A. Amara and A. Refregier, Mon. Not. Roy. Astron.

- Soc. **381**, 1018 (2007).
- [142] R. Bordoloi, S. J. Lilly and A. Amara, arXiv:0910.5735 [astro-ph.CO].
- [143] R. F. Quadri and R. J. Williams, *Astrophys. J.* **725**, 794 (2010).
- [144] F. Bernardeau, L. Van Waerbeke and Y. Mellier, *Astron. Astrophys.* **322**, 1 (1997).
- [145] L. Hui, *Astrophys. J.* **519**, L9 (1999).
- [146] A. Cooray and W. Hu, *Astrophys. J.* **548**, 7 (2001).
- [147] Takada, M., Jain, B., *MNRAS*, **348**, 897 (2004).
- [148] E. Sefusatti, M. Crocce, S. Pueblas and R. Scoccimarro, *Phys. Rev. D* **74**, 023522 (2006).
- [149] L. Van Waerbeke, arXiv:0906.1583 [astro-ph.CO].
- [150] T. Okamoto and W. Hu, *Phys. Rev. D* **67**, 083002 (2003).
- [151] W. Hu, *Phys. Rev. D* **64**, 083005 (2001).
- [152] K. M. Smith, W. Hu and M. Kaplinghat, *Phys. Rev. D* **74**, 123002 (2006).
- [153] K. Nakamura *et al.* [Particle Data Group Collaboration], *J. Phys. G* **G37**, 075021 (2010).
- [154] J. Smidt, S. Joudaki, P. Serra, A. Amblard and A. Cooray, arXiv:0909.3515 [astro-ph.CO].
- [155] Tegmark, M., *Phys. Rev. Lett.*, **79**, 3806 (1997).
- [156] L. Knox, *Phys. Rev. D* **73**, 023503 (2006). [astro-ph/0503405].
- [157] L. Knox, Y. S. Song and H. Zhan, *Astrophys. J.* **652**, 857 (2006).
- [158] R. Keisler, *et al.*, *Astrophys. J.* **743**, 28 (2011).
- [159] S. Joudaki, arXiv:1202.0005 [astro-ph.CO].
- [160] Knox, L., Scoccimarro, R., Dodelson, S., *Phys. Rev. Lett.*, **81**, 2004 (1998).
- [161] M. LoVerde, L. Hui and E. Gaztanaga, *Phys. Rev. D* **75**, 043519 (2007).
- [162] G. B. Rybicki, W. H. Press, *ApJ*, **398**, 169 (1992).